"Novel Drilling Technology Combining Hydro-Jet and Percussion for ROP Improvement in deep geothermal drilling"

This project has received funding from the European Union's Horizon 2020 research and innovation programme under grant agreement No 101006752

DELIVERABLE 5.1

"Report on Jetting with Different Mud Fluid Properties"

ABSTRACT

In preparation for simulation of the effect of the HPWJ on rock destruction during hybrid drilling, modifications to IC-FERST code solvers for non-Newtonian fluids were implemented together with rotating boundary conditions applicable to the geometry of planned jetting experiments. IC-FERST's LES turbulence solver was compared with UPC using a RNG k-ε model for HPWJ simulation. When identical nozzle outlet velocities were used for an axisymmetric static nozzle case with impinging plate boundaries to the domain of 3, 6 and 10 mm from the nozzle outlet, excellent agreement was observed for maximum impinging pressures. Experimental and numerical HPWJ studies in the literature are qualitatively in agreement with the ICL model but have differing setups and Re number, and therefore any differences observed cannot be explained with confidence. Further validation is anticipated when new pressure sensor results become available from ARMINES.

The model results for water are consistent with previous work. Impinging pressure in the core increases with chamber pressure and with small percentage reductions in magnitude. For jets with chamber pressure of 100 MPa, and nozzle diameter 1 mm the impinging pressure quickly converges to an almost constant value for stand-off distances of 3 mm and 6 mm, but for stand-off distance 10 mm, the flow is unstable. The effect of nozzle diameter requires future work with a fuller parametric study to include more conditions for a constant power delivered from the nozzle and at greater range of stand-off distances as well as for constant chamber pressure. Jetting with five fluid rheology models was simulated to explore the possible extreme effects of different fluids: drilling fluids at 50ºC, with 0%, 0.1%, 0.35% and 1% additives, and pure water at 20 ºC. The numerical results show that impinging pressure is not sensitive to the viscosity changes, a result that is consistent with the very high Re number regime.

Disclaimer

The present document reflects only the author's view. The European Innovation and Networks Executive Agency (INEA) is not responsible for any use that may be made of the information it contains.

DOCUMENT TYPE	Deliverable
DOCUMENT NAME:	D5.1. Report on jetting with different mud fluid properties
VERSION:	vfinal
DATE:	01/10/2021
STATUS:	S0
DISSEMINATION LEVEL:	PU

Authors, Reviewers				
Author(s):	John-Paul LATHAM, Jiansheng XIANG			
Affiliation(s):	Imperial College London			
Further Authors:				
Peer Reviewers:	Laurent GERBAUD, Hedi SELLAMI, Naveen VELMURUGAN (ARMINES)			
Review Approval:	Approved	Yes	Rejected (to be improved as indicated below)	
Remarks / Improvements:				

Version History			
Version:	Date:	Comments, changes, Status:	Person(s) / Organisation Short Name:
v0.4	24/09/21	First draft after internal review	JP Latham / ICL
v1.1	29/09/21	Final draft after peer review	JP Latham/ ICL
vfinal	01/10/21	Updated dissemination status from CO to PU	JP Latham/ ICL

Version Numbering	
v0.x	draft before peer-review approval
v1.x	After the first review
v2.x	After the second review
vfinal	Deliverable ready to be submitted!

Status / Dissemination Level			
Status		Dissemination Level	
S0	Approved/Released/Ready to be submitted	**PU**	Public
S1	Reviewed	**CO**	Confidential, restricted under conditions set out in the Grant Agreement
S2	Pending for review		
S3	Draft for comments	**CI**	Classified, information as referred to in Commission Decision 2001/844/EC.
S4	Under preparation		

TABLE OF CONTENTS

1 Introduction 4
1.1 Context and scope 4
1.2 Aims and Objectives 6
2 Background 6
2.1 Literature Review 6
2.1.1 Previous H2020 EU Projects 6
2.1.2 Theory 9
2.1.3 Experimental measurement of water jet velocity and impinging pressure 11
2.1.4 Numerical simulation of submerged water jet impinging pressures 12
2.2 Drilling Fluid Rheology 17
2.3 Summary of the problem to be simulated in WP5.1 19
2.4 Collaboration with Partners 20
3 The IC-FERST Numerical Model 20
3.1 CFD governing equation 20
3.2 Mesh adaptivity 20
3.3 Turbulence model 21
4 New code development 21
4.1 Implementation of non-Newtonian fluid law 21
4.2 Implementation of rotating reference frame for nozzle rotating with drill bit 21
5 Validation study - data for a deep wide domain (Jasper et al., 2021) 22
6 Applications 26
6.1 Domain (A) with Fixed HPWJ 26
6.2 Effect of chamber pressure on impinging pressure 32
6.3 Effect of stand-off distance SD on impinging pressure 32
6.4 Effect of nozzle diameter 35
6.4.1 Constant Chamber Pressure Case 35
6.4.2 Constant Power Case 36
6.5 Effect of non-Newtonian fluids 38
6.5.1 Viscometer Data 38
6.5.2 Curve-fitting model 38
6.6 Rotating nozzle simulation for Laboratory Rig - Domain (B) 42
7 Discussion and Conclusions 44
8 References 46
Appendix A 49

1 Introduction

1.1 Context and scope

In the ORCHYD project, the hybrid drilling technology is developed to improve the rate of penetration (ROP), which requires creating peripheral grooves using a high-pressure water jet (HPWJ) under the anticipated deep in-situ conditions. WP5 of the project focuses on understanding how best to optimise the action of the water jet to cut grooves as the bit rotates, using both experimental and numerical modelling methods. In parallel, the effect of groove geometry is studied in WP4 to modify the stress state for an easier rock failure under quasi-static and bit-hammer action conditions in the bottom-hole region. WP6 examines the hammering process for further analysis of the interaction of the HPWJ and percussive drilling in WP7. Finally, in WP8, a prototype hybrid system is built and tested. The environmental and social sustainability of the proposed technology is constantly evaluated throughout the project. The overview of the work plan and logic of ORCHYD are presented in **Figure 1**.

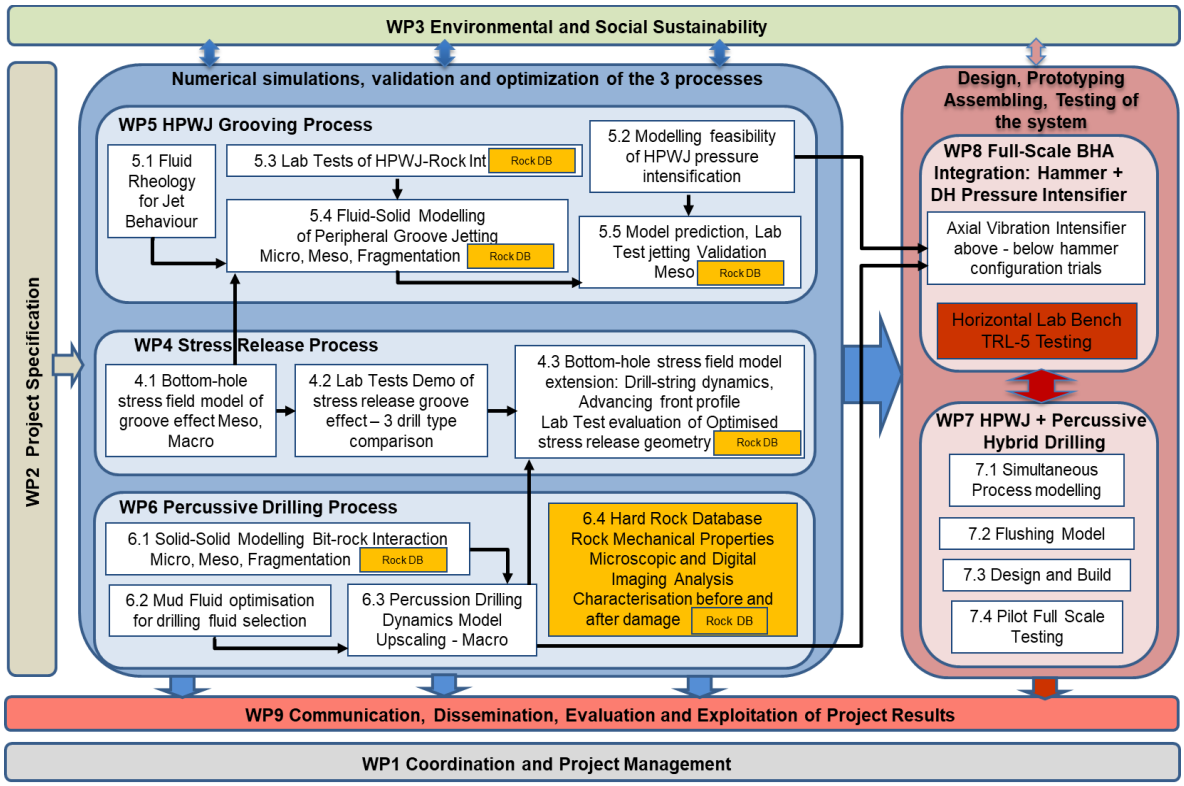

Figure 1. ORCHYD Project – Workplan structure.

WP5 has three main modelling components (WP5.1, WP5.2 and WP5.4) led by partner ICL to combine with laboratory HPWJ experiments on groove cutting in different rocks (WP5.3) led by partner ARMINES. The modelling aims to simulate rock breakdown and fragmentation under complex multi-physical fields/loads induced by the high-pressure fluid jet and hammer. Such a simulation tool will help to investigate a wider range of operational scenarios and rock types than those practical (or impossible in some cases) to test in the laboratory. The drilling is targeting deep ~4-6 km rock where it is more difficult to cut significant grooves. At such depth, in the bottom-hole where the drill chippings are mobilised before rising to the surface, the fluid pressure difference between that delivered to the nozzle chamber and the backpressure in the bottom hole (~50 MPa) needs to be ~170 MPa or greater (Stoxreiter et al., 2019). In fact, the operational conditions of the jetting system downhole needed to cut rock

grooves most effectively in different rock and in-situ conditions, which remain poorly constrained. WP5 targets this knowledge gap. Such extremely elevated jet pressure values require downhole pressure intensifiers to be integrated within bottomhole assemblies to deliver these extreme pressures to the orifice of the nozzle. The orifice diameters giving test results of most interest were determined to be between ~0.5 and 2.0 mm (Stoxreiter et al., 2018). However, it is not fully understood whether (i) the higher velocities associated with a smaller orifice will necessarily promote more rock destruction, and (ii) there are practical limitations of clogging if holes are too small. It is therefore important in this work when considering different nozzle orifice diameters that we investigate both the case of constant pressure (with velocity profiles that have the same average velocity) and the case when the nozzle delivers the same power but operating at different pressures and velocities for each different diameter nozzle. By performing the jetting experiments and simulations in this WP, the optimally positioned and sized nozzle(s) will be mounted near the rock-contacting front of the rotating hammer bit, near its periphery, to allow the shortest practical standoff distance and get the maximum benefit from the water jet's destructive action as it impinges and cuts into the rock surface to make a peripheral groove.

WP5.2 (led by partner UPC, with expertise in pressure intensifier designs) is applying computational fluid dynamics software to model the feasibility and suggested improvements to an intensifier design (Liao et al., 2015) that will be needed to deliver high pressures at 4-6 km depth downhole. As part of WP5.2, UPC has already modelled the intensifier, ultra-high-pressure tube with a precise nozzle design of interest deriving fluid flows everywhere upstream of the jet nozzle. Also, the jet itself and downstream flows into a simple axisymmetric volume domain were at the same time modelled by UPC to study impinging pressures on flat solid surfaces at different stand-off distances. In doing so, UPC delivered to ICL (authors of this report and partner modelling the fluid-solid rock interaction downhole, for the jet-rock destruction process in WP5.4) the required nozzle outlet velocity distributions, essential for further detailed study of bottom hole rock destructive power. For ICL's CFD models to be discussed in this report, these velocity distributions constitute the inlet boundary condition for fluid entering the computational domain. Two different computational volume domains are reported here for the range of steady high chamber pressures of interest between 100 and 250 MPa from the intensifier. These two domains are (A) an idealised axisymmetric non-rotating domain and (B) a domain based on the precise rig dimensions and rotating stage holding the rotating rock specimen (relative to a fixed nozzle), to be deployed by ARMINES in the HPWJ experiments of WP5.3.

Key fluid mechanics questions to answer early in WP5 (**Figure 2**) are:

i. what are the processes and predictable trends governing the interdependence of the controllable jetting parameters? taken here to include: nozzle chamber pressure, orifice diameter, stand-off distance, nozzle rotation (i.e. traversing rate), and the rheology of the jetting fluid itself.
ii. how do such operational parameters affect the magnitude of the impinging pressure, irrespective of the rock's resistance and state of stress?

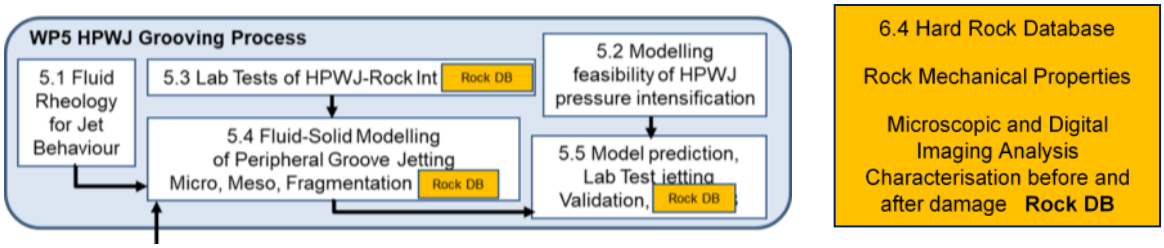

Figure 2. Structure of WP5. Work packages involving assessment of the hard rock suite to be considered are identified as the rock database assembled under WP6.4.

1.2 Aims and Objectives

The study's second aim is to develop the necessary preparatory enhancements to AMCG's in-house adaptive meshing code IC-FERST to meet the demands of the rock destruction drilling simulation tasks undertaken in WP5.4.

The properties of drilling fluids are often adjusted to fulfil certain functions that are considered advantageous for conventional drilling such as borehole wall stabilisation, chippings carrying capacity and wear reduction of mechanical parts. However, any significant change in effective viscosity and/or density, which results from fluid additives, may have a high impact on the impinging pressure and destructive energy that the jet can exert at a certain standoff distance. These changes potentially reduce or increase the jet's power and depth of groove cutting which would be of major importance to the project's success.

Therefore, the study's second aim is to put bounds on the likely effect of drilling fluid rheology on impinging pressures, considering pure water and a conventional composition mix of drilling fluid as the two base fluids. These two base fluids will be altered with a range of percentages of graphene oxide (GO) additives. The GO-modified fluids are being investigated by SINTEF, the research partner performing rheology and tribology research on drilling fluid with GO additives, in their work to examine the potential for drilling operation improvement including enhanced bit component durability and performance (WP6.2).

The objectives are:

i. to implement modifications to IC-FERST for non-Newtonian jetting fluid rheology
ii. to implement modifications to IC-FERST for a rotating reference frame of the nozzle with respect to the solid
iii. to validate the new IC-FERST model of HPWJ through a comparison with available literature
iv. to examine the effect on flow and impinging pressures of a range of nozzle orifice diameter, stand-off distance and nozzle chamber pressures for the extremes in drilling fluid rheology considered in ORCHYD.

2 Background

2.1 Literature Review

2.1.1 Previous H2020 EU Projects

There has been considerable interest in waterjet assisted drilling research in recent EU projects, with at least two main thrusts to improve geothermal energy exploitation potential.

The first focuses on a method of water-jetting and rock penetration using a multi-orifice nozzle which is unassisted by mechanical bit-rock interaction mechanisms. This method, designed to extend hydraulic and thermal connectivity between the main mother-bore well with the reservoir's hot fluids, aims to replace artificial stimulation mini-frack methods with a more environmentally friendly radial jet drilling (RJD) of multi-laterals using small diameter coil tubing. Success in the oil and gas industry with this RJD method has been reported for shallow multi-laterals in weaker sedimentary rocks. EC funded Horizon 2020 project "SURE" (Novel Productivity Enhancement Concept for a Sustainable Utilization of a Geothermal Resource), showed experimentally that water-jetting at 50 MPa jet pressure to extend a drill hole, whether by rotating or static nozzle jetting, will not overcome the ROP-suppressing effect of a bottom-hole back pressure of >15 MPa for relatively weak rocks (e.g. sandstone) with the uniaxial compressive strength (UCS) of 30-50 MPa, (Hahn et al., 2019). These experimental results were further supported by numerical simulation of jetting with solid fracturing. It was shown that for the single nozzle jet with the maximum velocity of 320 ms^{-1}, the sandstones were jet-able for zero back pressure, but with a modest increase in back pressure to 5 MPa, the fracturing hardly developed in rock with these sandstone properties (for details, see Xiang et al., 2019; Chen et al., 2021). Further effort to improve the nozzle design continues for such self-propelling self-rotary water jet 'bits' (e.g., Xiao et al., 2020). They investigate the position of the orifices at varying distances towards the extremity of the rotating nozzle and compare the rock breakage effect and bottom-hole pressure for different rotation rates, both experimentally and by numerical simulation of the impinging pressures. To overcome the threshold nozzle chamber pressures (needed to deliver effective ROP), the RJD method of creating laterals will require higher fluid pressures to be delivered downhole. For breaking harder rocks at depth, a pulsed water jet approach was shown to be more promising (Dehkhoda and Hood, 2013).

The second thrust towards future geothermal energy exploitation is to deploy the water jetting together with mechanical bit-rock interactions to create a new hybrid method of drilling. The idea that water jets might assist mechanical drilling has been around for half a century (Bobo 1963). A history of waterjet hybrid drilling research was introduced by Stoxreiter et al., 2018 together with their early results on kerf cutting experiments as part of a project to develop an alternative drilling system within the H2020 EU research project "ThermoDrill". Recognizing a hybrid system would need to operate with a certain rate of rotation of the bit, a measure of success of the jet's power to assist ROP was given by the depth of a groove or mass of material removed per unit time by the traversing jet (Stoxreiter et al., 2018). They investigated the key operational jet setup parameters (e.g., nozzle orifice diameter, nozzle chamber pressure, stand-off distance, traversing rate etc.) and determined the conditions for successful jetting and kerf cutting into a suite of hard rocks, mostly granites, for both ambient and a range of back pressures for a submerged jet. The focus of their experiments was to identify the jetting parameters which allow a satisfactory cutting performance under back pressures up to 45 MPa. Their results highlighted the effect of stand-off distance, back pressure, and jetting power on the depth of the groove, with some insights into the effect of nozzle type and drill fluid. This work was then integrated into a related Thermodrill study of jetting on a full-scale hybrid rotary mud drilling system (Stoxreiter et al., 2019). Some of their key results are summarized in **Figure 3**. The ROP of the rotary mud hammer increased by 50-60% because of introducing a 220 MPa pressure water jet mounted within the rotating bit. The figure also shows that the use of a xanthan gum drilling fluid led to a marginal ~10% reduction in ROP compared with a sepiolite-based drilling mud (an alternative clay to commonly used bentonite) that achieved results almost identical to clean water.

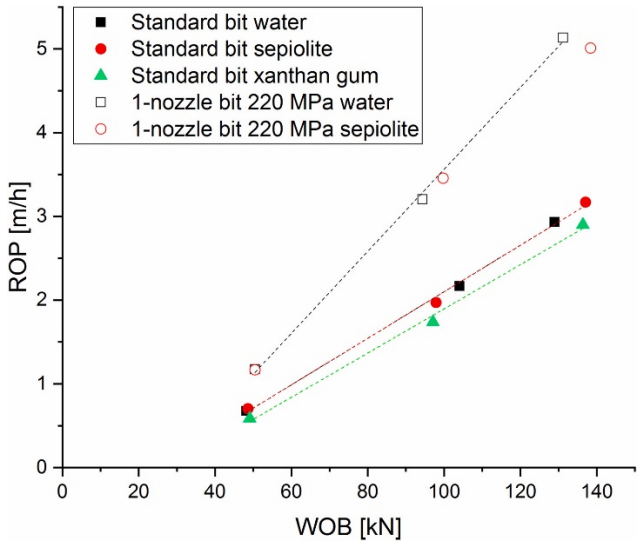

Figure 3. Indication of slight influence of drilling fluids on jet-assisted and unassisted rotary drilling (Stoxreiter et al., 2019).

The previous experimental work with water jet-assisted drilling has aimed to pre-condition and weaken the rock surface either by (i) cutting a peripheral groove down-hole, as in the case of rotary cutter drilling (Stoxreiter et al., 2019), or (ii) directing the jet more generally near to the points of bit-rock impacts of a hammering action drill, to enhance fracture network development (Liu et al., 2017). The optimal distance to either side of indenting disc cutters for kerf cutting by twin waterjets has also been investigated to enhance the performance of tunnel boring machines (Zhang et al., 2020). But for deep hard rock drilling, the overwhelming evidence is that kerfing any groove to a depth, which assists drilling, is much more difficult because of the role of higher bottom hole back pressures (~50 MPa at 5km depth). From simple theory, the increase in bottom hole drill fluid pressures generates increasing rock confinement and hence stress states are further removed from the rock's critical failure envelope criteria. Furthermore, experiments performing high pressure jetting into submerged rocks with a range of back pressures (Kolle, 1987; Poláček and Janurová, 2017; Stoxreiter et al., 2018) corroborate this theoretically predicted effect. However, the experiments suggest that it is possible to overcome 50 MPa of backpressure and the resistance to fracture of tough rocks like granites if: (i) a jet is from a nozzle chamber pressure with at least 220 MPa for the case of 50 MPa back pressure, (ii) there is enough power at the rock surface, and (iii) the jet does not transverse too fast. Cutting depths achieved as a function of standoff distance is shown for elevated back pressures, in **Figure 4**, where it is seen that standoff distance can be critical.

The need for safe operational pressures delivered from any surface works and inevitable pressure losses from pipe friction over great drilling depths means that the development of down-hole pressure intensification systems that can put sufficient power into the jet at ~4-6 km depths, has become a hot topic worldwide. Partner UPC is one such group pioneering intensification systems (Liao et al., 2015) with expertise in modelling the pressures and velocities achievable by different downhole pressure intensifier designs harnessing the energy in the drill-string and fluids.

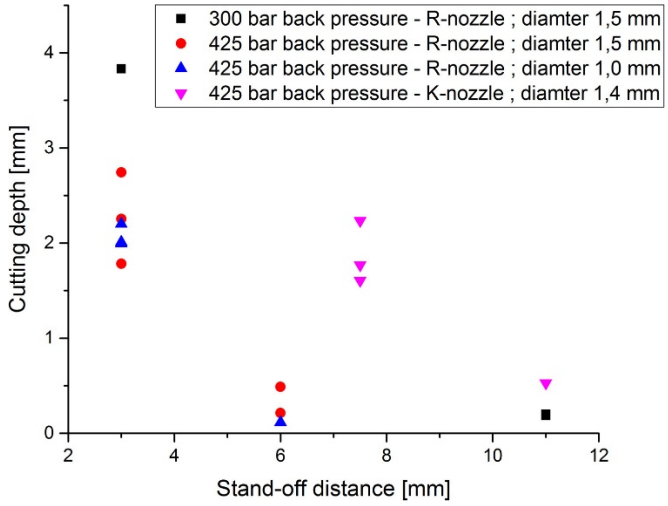

Figure 4. Kerf depth at constant traverse rate, featuring effect of stand-off distance but also back pressure and nozzle shape (Stoxreiter et al., 2018).

One practical concern investigated by Echt et al., 2021 is the ability of the drilling fluids to retain their properties over time. For this, there should be sufficient yield strength at slow shear rates needed to lift chippings together with low enough effective viscosity at high shear rates to limit dissipation of the jet's destructive energy. In the modelling research of WP5.1, we do not consider rate-dependent properties, nor loss of performance of drill fluid additives over drill time. The focus of WP5.1 is on understanding the potential destructive power of the jet (e.g., to cut grooves), and whether the different drilling fluid effective viscosities have any significant influence. The benefit of removal of already weakened rock fragments and lifting them away to avoid any unnecessary re-crushing of already broken material that can dampen the breaking action is to be considered in connection with a significantly slower velocity of flushing, in WP7.

2.1.2 Theory

To understand HPWJ in submerged impinging plate geometries, the jet theory momentum solution for turbulent jets of Schlichting, 1979 is widely referenced together with the experiments of Hussein et al., 1994, which we assume here to be of a fully developed cylindrical flow velocity profile emerging into a stagnant large domain. The laser-Doppler anemometer (LDA) results of Hussein are for air, which has approximately one thousand times lower viscosity than liquid. The loss of jet velocity axially and radially in the air is generally considered applicable to submerged liquid flows for cases of similar Reynolds number (Re) and therefore flow regime, for turbulent jets.

Re, which characterises the ratio between inertia and viscous forces can be estimated easily for a water jet at 20 ^{o}C, with the density of 1000 kg/m^3, the dynamic viscosity of 1 mPa.s and orifice diameter of 1 mm with jet average velocities of 450 to 700 ms^{-1} to be 450,000-700,000 (i.e., strongly turbulent).

More typically, flows in long cylindrical pipes with boundary layer effects will establish a parabolic form near the wall in the profile plane and such fully developed flow profiles are often taken as boundary conditions for entry velocity for such investigations. However, for the case of HPWJ numerical investigations of nozzle jet flows with just a short distance to the outlet after the convergent cone in the nozzle, a constant planar velocity or top-hat profile may be a more appropriate distribution to choose for the initial orifice entry velocity.

Figure 5a shows the axial velocity normalised by the maximum velocity at the centre of the jet inlet plotted against the radial distance for many different sample axial distances into the domain but normalised by the jet's half width $r_{½}$ (i.e. radial distance for which the velocity has fallen to half the axial value). The experimental data then collapses onto the one curve. **Figure 5**a illustrates the mean jet entry velocity divided by the centreline velocity at different axial distances into the domain (scaled to the nozzle diameter) based the data in (Hussein et al., 1994).

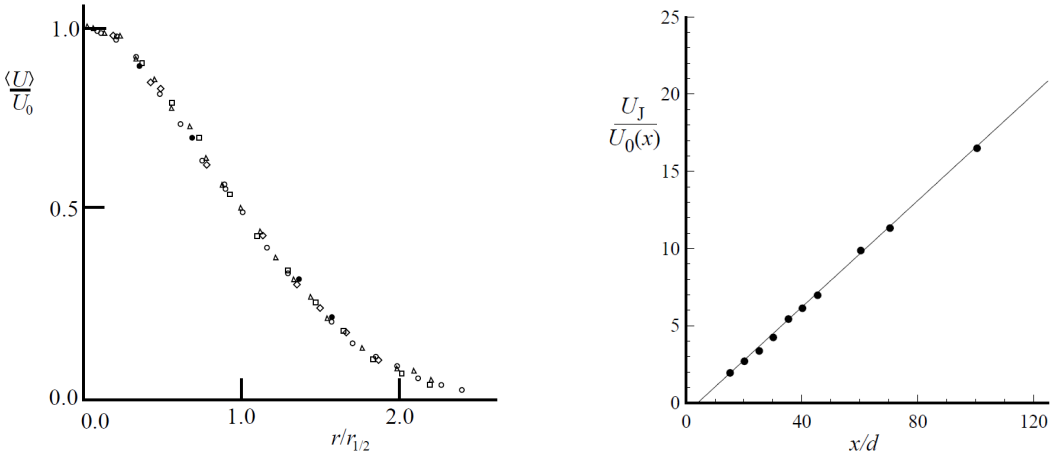

(a) *(b)*

Figure 5. Plots to explain turbulent conical jet theory (Pope, 2000).

The form of Hussein et al's bell-like curve, for *Re* = 95,500 is fitted by the equations:

$$r_{1/2}(x) = S(x - x_0) \quad (1)$$

$$\frac{U_0(x)}{U_J} = \frac{B}{(x - x_0)/d} \quad (2)$$

with spreading constant S defining the jet's half-width and with intercept x_0 defining the virtual origin with $x_0/d = 4$ and $B = 5.8$ being an empirical constant. Pope also discussed the startling evidence from experiments with Re of 11,000 and 95,500, together with references reporting Re 1000 times larger than this range, that the self-similar shape is retained, and the velocity decay constant B (~5.8) and the spreading rate S (~0.094) do not vary significantly with Re for this wide range of high *Re* values.

The velocity distribution transformations given by **Equations 1** and **2** that were plotted in (Hahn et al., 2019) are given in **Figure 6** for an orifice diameter of 2 mm and maximum velocity of 320 ms^{-1}, (average velocity = 160 ms^{-1}) and a jet entering an infinite quiescent domain. Profiles are at different axial stand-off distances, L, as multiples of nozzle diameter. Here, we illustrate that the maximum velocity at axial distance expressed as L/d between 3 and 5 is already reducing substantially, according to the theory and empirical fits from experiments with air jets by Hussein et al., (1994).

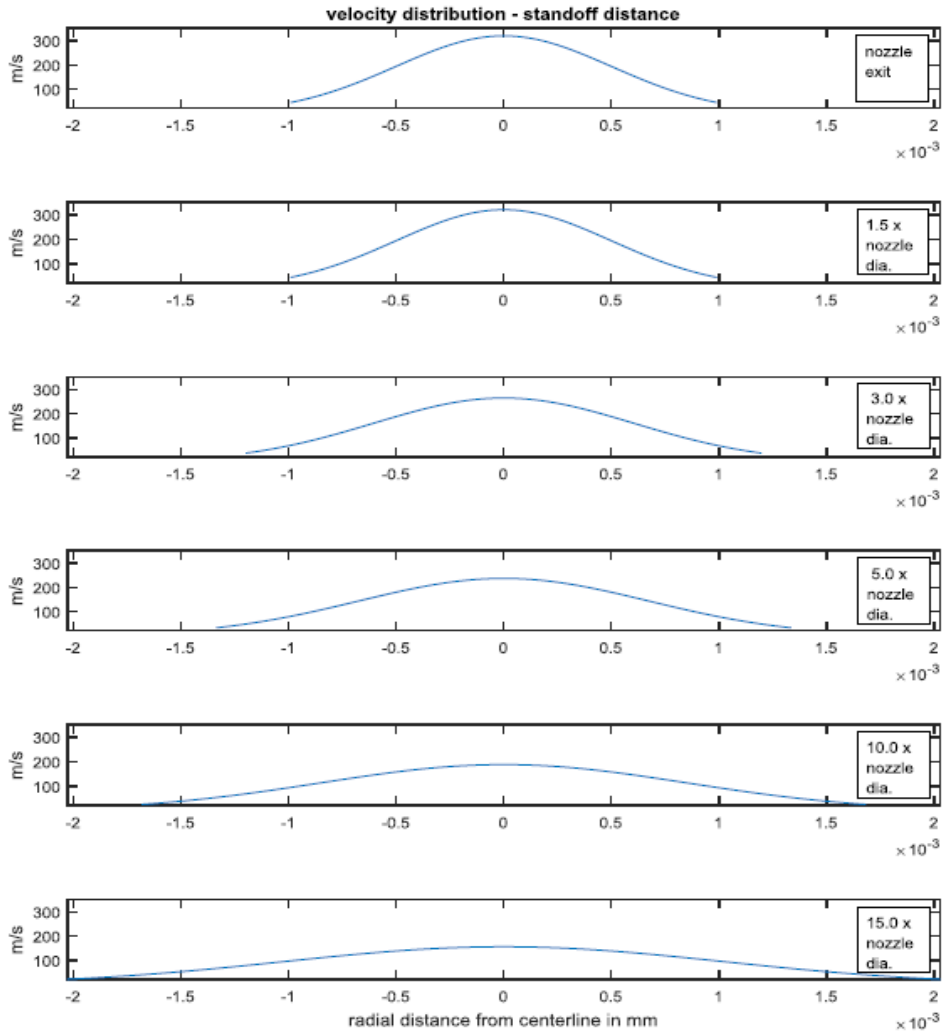

Figure 6. The velocity distribution for a HPWJ in submerged conditions, calculated according to **Equations 1** and **2** (Pope, 2000; Hahn et al., 2019b).

2.1.3 Experimental measurement of water jet velocity and impinging pressure

There had been little experimental validation to prove that such a theory applies to submerged water jets until Zhang et al., 2011 directly measured submerged water jet velocities with Particle Image Velocimetry (PIV). Again, there is no impinging plate nearby for this case where a 5 mm orifice enters from a pipe that penetrates 100 mm into the domain of ~300 x 300 x 300 mm, and interestingly, the Gaussian type distribution measured by PIV is a good match to the theory and results for air reported by Hussein. Jasper et al., 2021 recently performed PIV for velocity distributions using two different nozzles, one generating cavitation inside the nozzle. Tests were performed over a range of back pressures to evaluate both the kinematic effect of the jet and the regime where cavitation bubbles can exist.

An alternative means to characterise and validate the effect of jet flows is to measure pressures directly and to mount pressure sensors in the jet path. Most success has been achieved with piezoelectric film (PVDF) sheets (see e.g., Jegaraj and Babu 2016; Sittiwong et al., 2010), but these are prone to be damaged by the exceptional pressures of jets striking the sensor components, especially studies focussed on pulsed jets and the water hammer effect (see Dehkhoda and Hood, 2013).

Confidence in predicting erosive power and depth of cut from theory and experiments for velocity distributions and associated impinging pressures at different distances into a stagnant large domain is questionable given that: the bottom hole domain of interest may have a very short distance between nozzle exit and planar solid obstruction opposite the jet. The drilling fluid's effective viscosity under jetting action may not be Newtonian and may be poorly represented by viscosity determined at shear rates below 1000 s^{-1}. Furthermore, having a jet entry position traversing rapidly because of its attachment to a rotating drill may inhibit full impinging pressure development on the solid surface that is predicted by a theory that, to date, has not accommodated cases for jet entry very close to the solid.

2.1.4 Numerical simulation of submerged water jet impinging pressures

A wide-reaching review of water-jet simulation by Liu et al., 2019 covers mainly industrial machining, cutting, milling, and cleaning applications mostly with abrasive additives and in air, but provides an insight into the range of jet-solid interaction models that are under development including cutting of rock. Liu et al. highlighted one FEM CFD model by Maniandaki et al., 2007 that was used to generate impinging pressures on polyurethane-coated aluminium. The pressure profile obtained is applied as boundary conditions to simulate the fluid-induced stress and damage in the solid domain (i.e. rock), in which the solid removal criterion is based on a threshold strain. They modelled the water inside the nozzle, after exiting the nozzle (into the air), and the impinging flows to investigate a nozzle diameter of 1 mm and jet velocity of ~500 ms^{-1} which is in the range of interest to ORCHYD. Their workflow is given in **Figure 7**. **Figure 8** shows the details of nozzle velocity profile development upon entering uniformly at 100 ms^{-1} and exiting the convergent accelerating zone along a focussing stabilization length of tube that gives a fully developed stable profile on exiting at ~1200 ms^{-1}. The profile goes through a flat fronted top hat profile just after the convergent zone and stabilises after 30 mm to a less sharp but still quite flat fronted profile on entering the air region.

Impinging jet numerical model studies tend to focus on air jets and thermal transfer research and remarkably only a few studies have considered submerged impinging water jets. One recent study on the erosive scouring action on subaqueous sediments by Wang et al., 2020 stands out as highly relevant as the application is in many respects aligned with the objectives of WP5. Their study domain, while using a much larger diameter jet pipe of D = 20 mm and lower velocities of about 1 ms^{-1}, considered the Re range of flows of $11{,}700 \leq Re \leq 35{,}100$ – not very much below those expected to be delivered in the jetting tests in WP5.3 with Re of say 500,000 to 700,000. The standoff distance effect on impinging pressure was studied by bringing the central pipe outlet further and further into a large rectangular computational domain of stagnant water with depth H = 8D, with distant outflow boundaries and the full water depth H_w = 12D as shown in **Figure 9**. The velocity profile for outflow at the exit of the pipe is assumed to be a fully developed pipe profile.

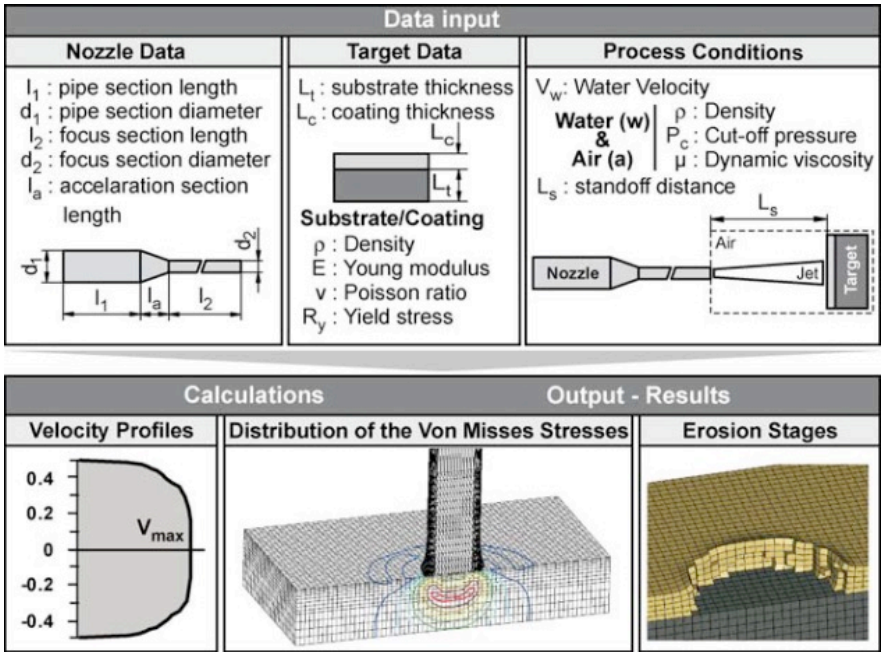

Figure 7. Flowchart of the jet erosion modelling (Maniandaki et al., 2007).

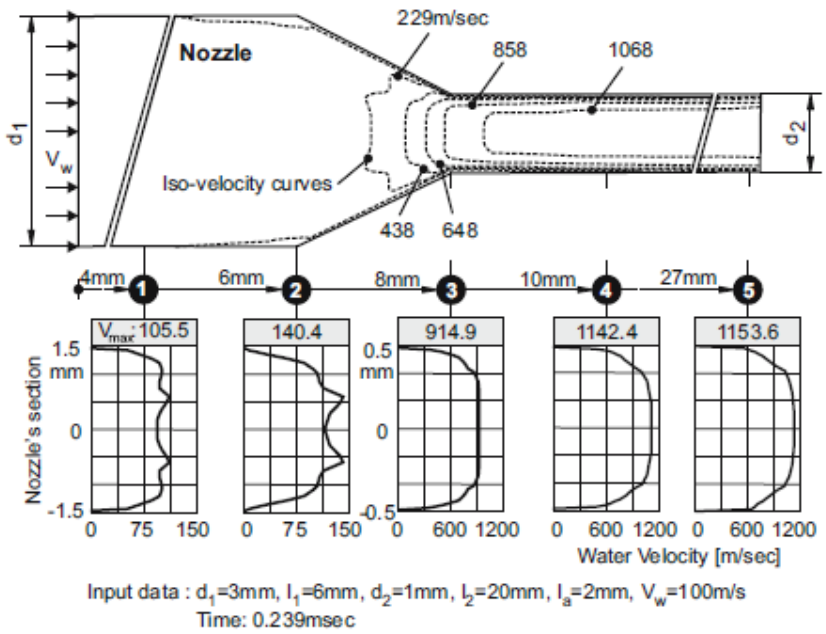

Figure 8. Detailed results of velocity profile development in a nozzle with stabilisation length, (Maniandaki et al., 2007).

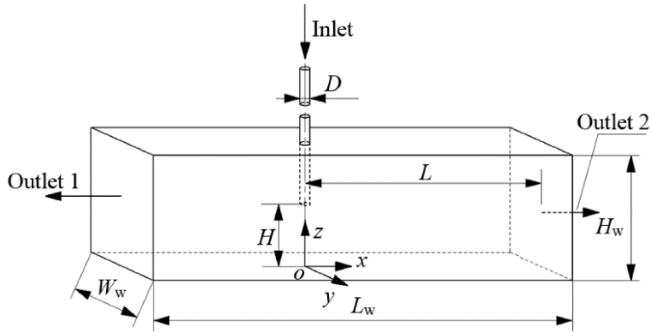

Figure 9. Computational domain set-up (Wang et al., 2020).

They showed that from six different types of turbulence capturing schemes, the Wray-Argawal (W-A) method gave the best fit to the air chamber experimental profiles measured with a PIV method and reported in (Fairweather and Hargrave, 2000) and where the same range of Re was considered (Re~18,800). For a fully developed circular jet, Fairweather and Hargrave found the experimental profile was quite well fitted by the empirical formula $V/V_{max} = (1-2r/D)^{1/n}$, with n = 7, where V was the local velocity at any position, V_{max} was the maximum velocity at the jet exit and r represented the radial distance. The average or bulk velocity at the jet exit, V_b, can be defined as $V_b = 4Q/\pi D^2$ (Q is the volume flow rate of the jet). Using W-A, Wang et al. apply the fully developed velocity profile as a boundary condition at the end of the pipe as water enters, so for the case of H/D = 8, the jet is far from abutting against the opposite wall and the axial and radial velocity profiles can be expected to fit well with the theory and experiments that consider jet entry into large unlimited domains. The results are shown in **Figure 10**.

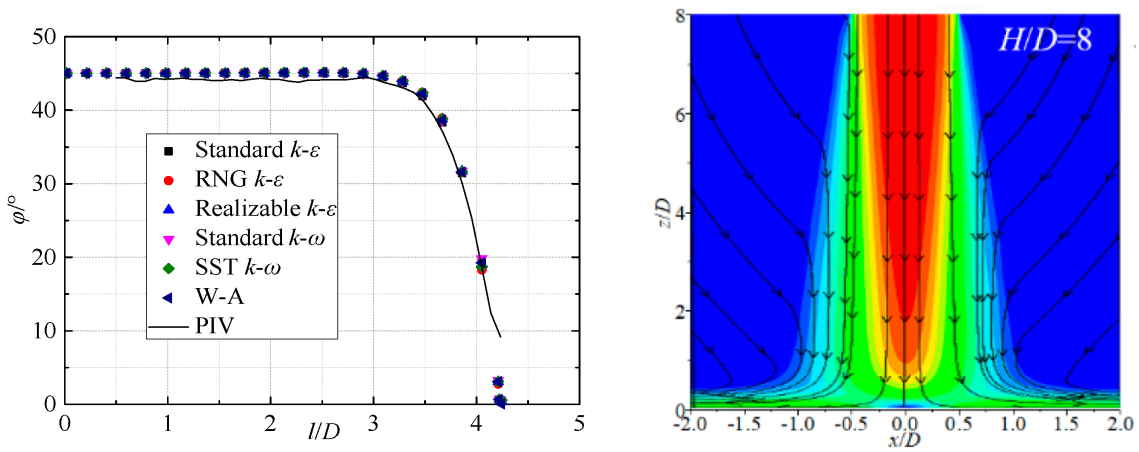

(a) *(b)*

Figure 10. Scaled velocity computed along jet axis with scaled axial distance *l*/D from the exit, for jet entry condition far from the opposite plate boundary (H/D=8) (Wang et al., 2020).

The jet core loses its power between about 3 < *l*/D ≤ 4.24. If the jet emerges just 3D from the impinging plate (i.e., H/D=3 which is equivalent to a stand-off distance of 3 mm for D=1 mm). **Figure 11**a shows the H/D =3 case with strong deflection of streamlines near the plate that results in a change of velocity profile and associated impinging pressures. The horizontal profiles shown in **Figure 11**b are sampled at various distances from the plate and the velocity dip in the stagnation high-pressure zone is shown clearly for z/D = 0.05.

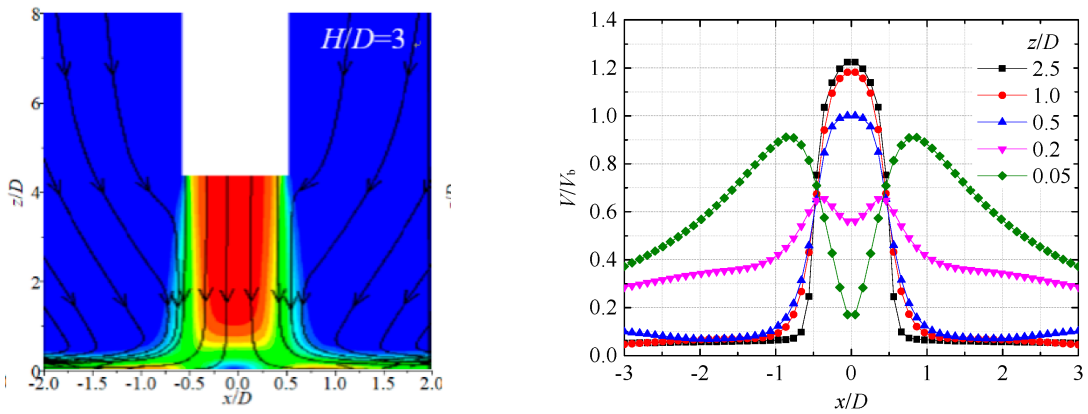

(a) *(b)*

Figure 11. Model results for H/D = 3 (Wang et al., 2020).

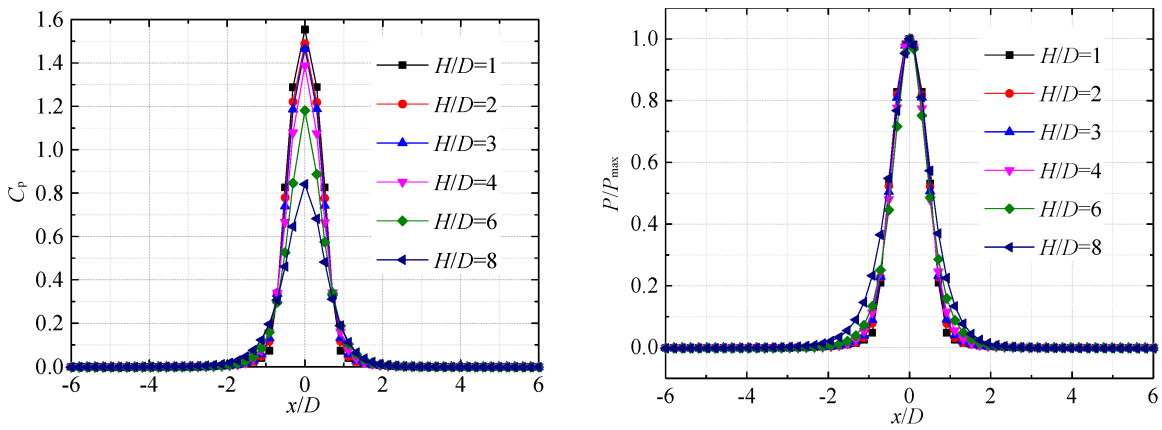

(a) *(b)*

Figure 12. Model results (Wang et al., 2020): (a) impinging pressure coefficient C_p and (b) normalised pressure P/P_{max} with variation along the x axis in the flow direction.

In **Figure 12**, the variation with x of the impinging pressure coefficient C_p representing pressure as a proportion of the jet pressure at the nozzle, calculated using bulk velocity, is shown for each standoff distance. Furthermore, Wang et al provide a function for the maximum impinging pressure coefficient that best fits their simulation results for the peak impinging pressure built up directly beneath the stagnation zone and exerted on the plate, as a function of H/D given by the equation in **Figure 13**. For this plot, C_{pmax} given by:

$$C_{pmax} = (P_{max} - P_0)/0.5\rho V_b^2 \quad (3)$$

can be considered the maximum pressure in relation to an initial static pressure or back pressure P_0, that can be directly scaled by the jet pressure associated with the kinetic energy per unit volume introduced by the jet.

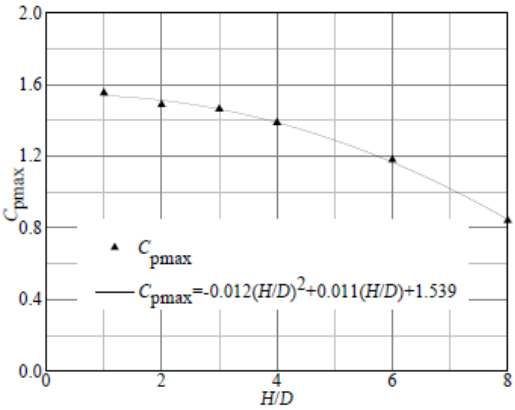

Figure 13. Simulation results and predictive equation best fit to numerical results (Wang et al., 2020).

To predict the erosive power of a jet, it will also be important to consider not just the maximum impinging pressure but also the area over which it acts, and this was also illustrated in the results of Wang et al. (**Figure 14**). In addition to the steady or dynamic impact pressure in the impingement region (i.e. a stagnation zone of elevated pressures as shown in **Figure 15** for the flat smooth plate), the radial wall jet region of deflection and high shear rate next to the target surface may also provide a destructive mechanism, especially for rough surfaces.

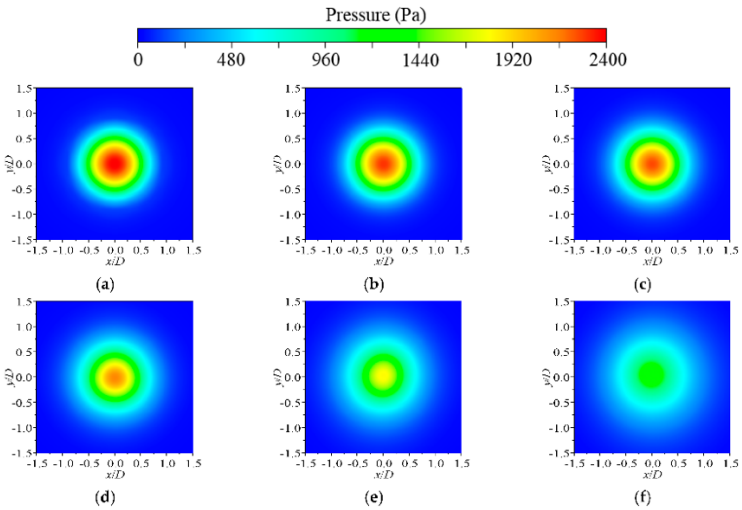

Figure 14. Pressure contour on the impinging plate with the jet entry positioned at various impinging heights (Wang et al., 2020): (a) H/D = 1; (b) H/D = 2; (c) H/D = 3; (d) H/D = 4; (e) H/D = 6; (f) H/D = 8.

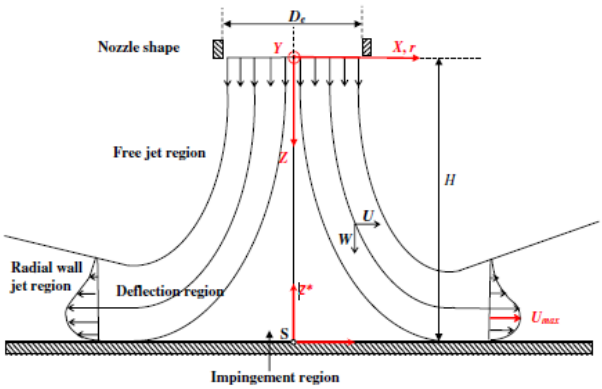

Figure 15. Regions of an impinging jet (Sodjavi et al., 2015).

The effect of a traversing water jet entering stagnant water was studied using the experiments (**Figure 16**) and numerical simulation (Xiao et al.,2020), where the interest is at large distances from the nozzle. However, their numerical results revealed that to minimise the deflection effect of a traversing jet, the strong jet force was required while considering how close the jet was to the solid.

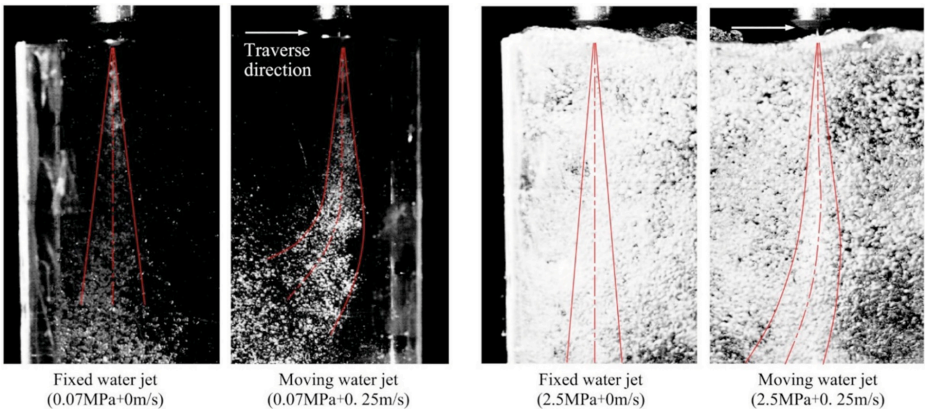

Figure 16. Study of traversing effect on deflection of jet (Xiao et al., 2020).

It should be noted that the role of cavitation bubbles, whether to block flow velocity in the jet core or to provide bubble burst assistance to erosive jet action is not considered in the work of WP5. HPWJ kerf cutting experiments and simulations will be performed for significant confinement and backpressure levels where calculation of the cavitation number suggests jetting is likely to exclude cavitation phenomena, as explained in (Jasper et al., 2021) and discussed also in (Stoxreiter et al., 2018; Kolle 1987). However, Li et al., 2014 caution against using the cavitation number to dismiss possibilities of there being some active effects, without further recognition of the implicit assumptions. They imply that cavitation bubbles could potentially be created at depth (~3 km) if a self-vibrating nozzle can sufficiently reduce local pressures. Thus, they suggest that further experimental work is required as cavitation bubble bursting is recognised for enhancing jet erosion in atmospheric conditions.

2.2 Drilling Fluid Rheology

The literature on drilling fluid rheology, often termed drilling mud rheology, spans a huge range of shear rates of interest – the textbook 'Composition and Properties of Drilling and Completion Fluids' provides informative background (Caenn et al., 2017). In a recent critical review (Agwu et al., 2021), this range of shear rates was illustrated as shown in **Figure 17**, with different ratios of Yield Point to Plastic Viscosity.

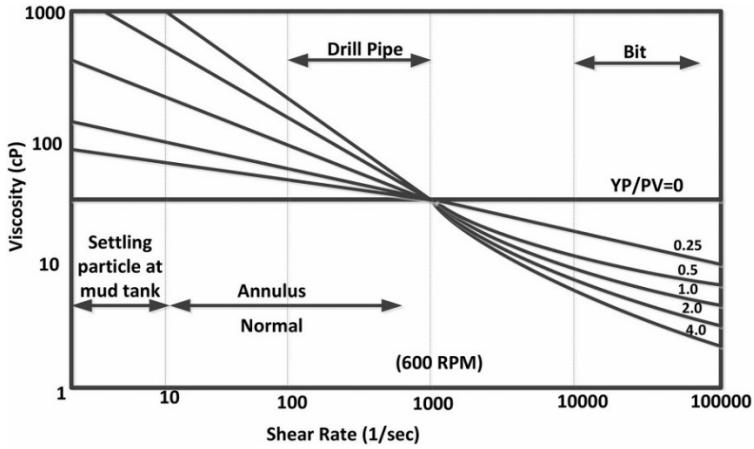

Figure 17. Range of shear rates of interest in typical drilling operations (Agwu et al., 2021).

Echt et al., 2021 report the power-law fit for xanthan gum and sepiolite drill fluids for shear rates up to 1000 during the Thermodrill waterjet assisted rotary drilling experiments, concluding: "in various geothermal drilling operations when water cannot be used as drilling fluid due to limitations concerning borehole stability, carrying capacity and others, the sepiolite drilling fluid poses a highly interesting and promising alternative". Because the focus of this work in WP5 is on fluid behaviour that may influence jetting performance, rheological models capturing the non-Newtonian behaviour for the very high shear rates 10^3-10^6 of interest need to be considered. If the jettability is shown to be insensitive to effective viscosity inside the intensifier and jet nozzle, drill fluids that could be selected and improved for operation can then take advantage of other functions of drilling fluid such as given by a higher Yield point. There is very little literature on drill fluid rheology related to its jetting performance, however Kristiawan et al., 2015 highlight the type of rheological changes with nano-particle additive concentrations in water at relatively high shear rates possibly applicable to jetting applications where their objective is in seeking improved cooling properties. A modified power-law model is preferred to characterise their non-Newtonian results (see **Figure 18**) for such shear rate thinning fluids (power-law exponent < 1) which is discussed in their paper.

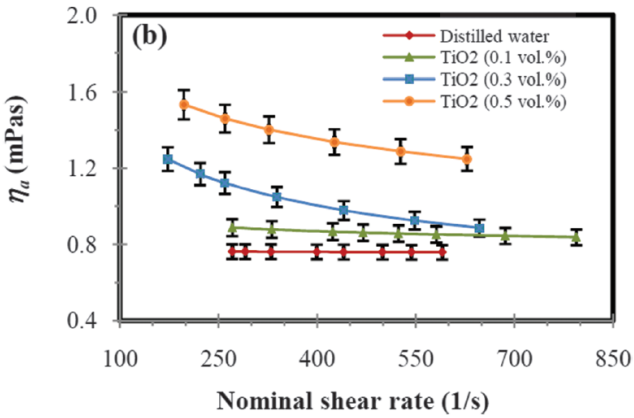

Figure 18. Typical rheological trends observed in water base fluid with nano-sized particle additives. (Kristiawan et al., 2015).

2.3 Summary of the problem to be simulated in WP5.1

The WP5 scope is to investigate HPWJ efficiency experimentally with a limited range of alternative, potentially exploitable, advanced fluids that use GO additives. The range of percentage by weight additive will need optimising for the two base fluids: water, or a regular recipe based on bentonite xanthan gum. The fluid temperature will be set to 50-60 degrees Celsius to be consistent with the realistic downhole temperature of fluids. The effect of the changes in fluid rheology is best explored based on direct experimental measurement (a task undertaken by SINTEF). Numerical models can then assess the extreme bounds of behaviours resulting from the rheology for this range of additives and base fluids.

The experimental HPWJ sensitivity study (ARMINES WP5.3) will focus on a parameter range for nozzle chamber pressure (100-250 MPa), standoff distance (~2-10 mm), orifice diameter (0.5-2.3 mm), backpressure (30-50 MPa) guided by extensive recent work on kerf cutting performed during the EU project Thermodrill. The one nozzle type selected for experiments (Karcher Forme1) is based on a convergent circular design reported giving effective rock cutting results and allowing a full range of nozzle diameters. Nozzle design optimisation is not within the scope of the simulation research in WP5.1 of ORCHYD. However, review of available data has supported the nozzle design choice for the base case geometry and further nozzle geometry experimentation may be included in WP5.3.

For an HPWJ entering a domain of depth greater than 8D, the theory has suggested the powerful core of the jet would extend to a standoff of at least 6.5 D (Kolle, 1987). However, a recent key simulation study (Wang et al., 2020) with similarly high Re and a Newtonian fluid model indicated that the flows were different when the domain depth ahead of the jet was much closer and that the maximum impinging pressure may drop off considerably, by 10% at 4D and by ~20% at 6D. The theory also suggests that the kinetic energy per unit volume delivered at the nozzle will be a determining factor for the maximum impinging pressure that is then moderated by the dissipation effect due to standoff distance.

Numerical modelling planned for WP5.1 is designed to prepare for the WP5.4 task to reproduce the planned rock kerf cutting experiments as nearly as is practically feasible with AMCG's modelling software platform, IC-FERST. For validation, the accuracy of the IC-FERST jetting simulation is best studied using both: (i) a comparison of IC-FERST simulations of Newtonian fluid CFD appropriate for water and any reported in the literature, and (ii) a direct comparison with new experimental studies using a novel sensor design that can be positioned at the impinging plate. Both non-Newtonian behaviour and the short length of the nozzle orifice following the convergent zone with a non-fully developed velocity profile can influence the velocity profile entering the bottom-hole computational domain. This velocity distribution must be given as an input for further coupled modelling of fluid-solid interactions with a rotating nozzle to be solved. These velocity distributions have been provided already by UCP in an internal report titled "Nozzle simulation results" using a Newtonian viscous model and for the nozzle geometry and chamber pressures of interest for the experiments and hence simulations.

For the tasks of WP5.1, there are two computational domains of interest to be modelled, each assuming 'Karcher Forme1' nozzle type. Domain (A) is an axisymmetric geometry that is easily compared with theoretical cases, laboratory experiments and simulation results from the literature. Domain (B) is based on the geometry of the experimental rig and has a nozzle entry point offset from the centre that rotates at rates compatible with the intended hybrid drilling technology. In this report, the effects of drilling fluid and setup conditions on impinging

pressures are explored for Domain (A), while the feasibility of modelling a rotating jet is proven for Domain (B).

2.4 Collaboration with Partners

The work contained in this report has included input from colleagues as follows:

i. Extensive discussions on the range of parameters, nozzle geometry, testing rig geometry, to be the subject of jetting experiments in WP5.3 (ARMINES)
ii. Extensive discussions on choice of drilling fluids to consider for modelling (ARMINES/SINTEF)
iii. Data with results of testing of rheological properties and assistance with data interpretation for the target types of drilling fluids (SINTEF)
iv. Numerical modelling of the flow into the nozzle, acceleration within it and jet response upon exiting into a quiescent domain, to determine a set of exit velocity distributions to be used by ICL's models, and a set of impinging pressure results to be used as a further validation data set for ICL's models. Short report made available (UPC)

3 The IC-FERST Numerical Model

3.1 CFD governing equation

IC-FERST, an open-source finite-element CFD model, is used here to model the high-speed water jet. It is a general purpose CFD code capable of modelling a wide range of fluid phenomena involving single and multiphase flows. The IC-FERST project's history has led to several novel advanced methods based upon adapting and moving anisotropic unstructured meshes, and advanced combined finite element and control volume (CVFEM) discretisation.

In this report we first describe the existing CFD model before progressing to the code and application developments added here to address the rotary jet drilling application in ORCHYD.

The continuity equation is:

$$\nabla \cdot \mathbf{u} = 0 \tag{1}$$

Where **u** is the fluid velocity.

The momentum equation is given as follow:

$$\rho \left(\frac{D\mathbf{u}}{Dt} + \mathbf{u} \cdot \nabla \mathbf{u} \right) = -\nabla p + \nabla \cdot \mu (\nabla \mathbf{u} + \nabla^T \mathbf{u}) + \rho \boldsymbol{g} \tag{2}$$

where ρ_f is the fluid density, p is the fluid pressure, μ is the fluid viscosity, g is gravity. In the ORCHYD project, drilling fluids and water are treated as incompressible fluids. The temperature has a small effect on water density, i.e., water density decreases from 1000 kg/m^3 to 988 kg/m^3 when the temperature increases from 20°C to 50°C, resulting in 1.2% difference. In this work, we use constant density, 1000 kg/m^3.

3.2 Mesh adaptivity

To reduce CPU cost without loss of accuracy, the dynamic mesh adaptivity can be used for application of HPWJ. The grid adaptation scheme used here is based on the anisotropic grid optimization library of Pain et al. (2001), in which two different techniques can be combined to

change elements: mesh refinement or "h" method; and node relocation or "r" method. In this study, we used it for dynamic mesh optimisation (DMO).

In this study, we used adaptive times-step scheme to dynamically adjust the size of the time-step. The size of the time-step is linked with the Courant-Friedrichs-Lewy (CFL) number.

3.3 Turbulence model

To deal with turbulent flow and associated numerical instabilities, an implicit sub-grid scale filtering through a Smagorinsky's model (Smagorinsky, 1963) is used to discretise the momentum equations. An explicit Large-Eddy Simulation (LES) turbulence model is also implemented within the adaptive meshing approach of the modelling framework; while considering the variability of the adaptive mesh element spatial dimensions, the filter is additionally allowed to vary in space and time. Additionally, in order to add further stabilisation, the Petrov-Galerkin method (Tezduyar, 1991, Pain et al. 2001, Hughes and Mallet, 1986) is also applied to the momentum equations, using an upwind weighting of the equations and an additional diffusion term in the di-rection of the gradient of the solution.

4 New code development

4.1 Implementation of non-Newtonian fluid law

To implement non-Newtonian law, we first calculate the shear rate as follows

$$S=1/2(\nabla\mathbf{u}+(\nabla\mathbf{u})^T) \qquad (3)$$

Where S is the shear rate in the format of tensor, $\nabla\mathbf{u}$ is the velocity gradient.

If the effective viscosity μ_{eff} is isotropic, then we use absolute value of maximum S(:,:).

$$\mu_{eff}(::) = k_1 S(::)^{n_1} + k_2 S(::)^{n_2} \qquad (4)$$

If the effective viscosity is anisotropic tensor,

$$\mu_{eff}(::) = k_1 |S(::)|^{n_1} + k_2 |S(::)|^{n_2} \qquad (5)$$

4.2 Implementation of rotating reference frame for nozzle rotating with drill bit

As the nozzle is rotating, we need take the transverse velocity into account. The velocity components, u, v, w in x, y, and z directions are calculated as follows.

$$x_p = \mathrm{L}\cos\omega t \qquad (6)$$

$$z_p = \mathrm{L}\sin\omega t \qquad (7)$$

$$D_{c,p} = \sqrt{(x - x_p)^2 + (z - z_p)^2} \qquad (8)$$

$$\begin{cases} if\ D_{c,p} \le R_n \quad u = -\omega(z - z_c) \\ \qquad else \quad u = 0 \end{cases} \qquad (9)$$

$$\begin{cases} if\ D_{c,p} \leq R_n \quad v = specified\ axial\ velocity\ profile \\ \qquad\qquad\qquad else \quad v = 0 \end{cases} \tag{10}$$

$$\begin{cases} if\ D_{c,p} \leq R_n \quad w = \omega(x - x_c) \\ \qquad\qquad else \quad w = 0 \end{cases} \tag{11}$$

$$u = -\omega(z - z_c) \tag{12}$$

$$w = \omega(x - x_c) \tag{13}$$

where x, z are the coordinates of a point on top boundary in x and z directions; x_p and z_p are the coordinates of center of nozzle in x and z directions at time t; x_c and z_c are the coordinates of rotating center; Dc,p is the distance between the point and rotating center; ω is the angular velocity.

5 Validation study - data for a deep wide domain (Jasper et al., 2021)

Jasper et al., 2021 present velocity results from PIV measurements with three different nozzles, one of which is a convergent cone nozzle with orifice 2 mm. The large volume stagnant domain PIV results for given chamber pressure and back pressure, where flows are outside the range of cavitation, provide an opportunity to compare our IC-FERST results with experimental data. The experimental data presented is after a steady state jet is established and the velocimetry results showing radial variation (y/d) are available for 2D slices at different axial distances (x/d) from the outlet.

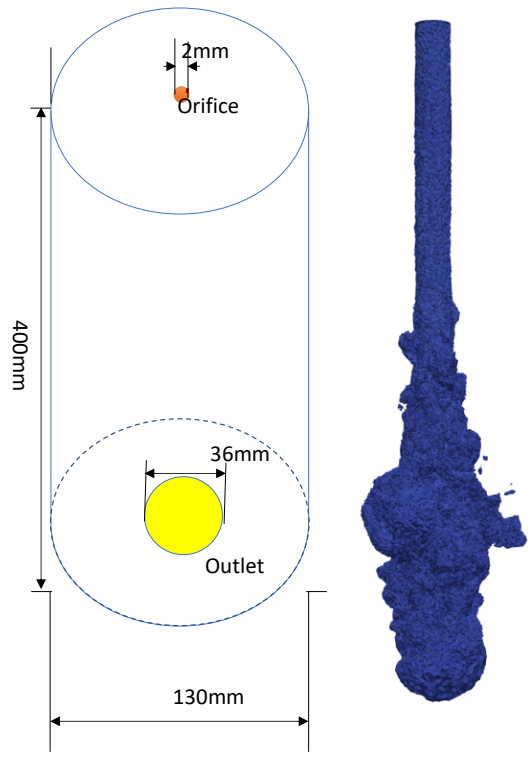

Figure 19. IC-FERST (a) Schematic of simulation setup; (b) jet shape after removal of all elements for which the fluid velocities are less than 10 m/s.

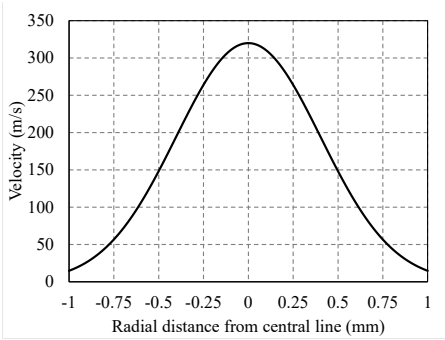

Figure 20. Profile of fluid exit velocity distribution in the water jet (Hahn et al., 2019b).

The fluid domain of the long pipe problem of Jasper et al. (length 0.13m, diameter 0.13m) is initially filled with fluid with a pressure of zero and has a boundary condition of $p = 0$ at the outlet (yellow circular area in **Figure 19a**). A velocity boundary condition with the profile given in **Figure 20** is applied at the orifice (red circular area in **Figure 19a**) and maintained during the simulation, once started. The rest of the boundaries are applied with no-slip boundary conditions. **Figure 19b** shows the submerged jet shape at 440 µs after all elements for which water velocities are smaller than 10 m/s have been excluded.

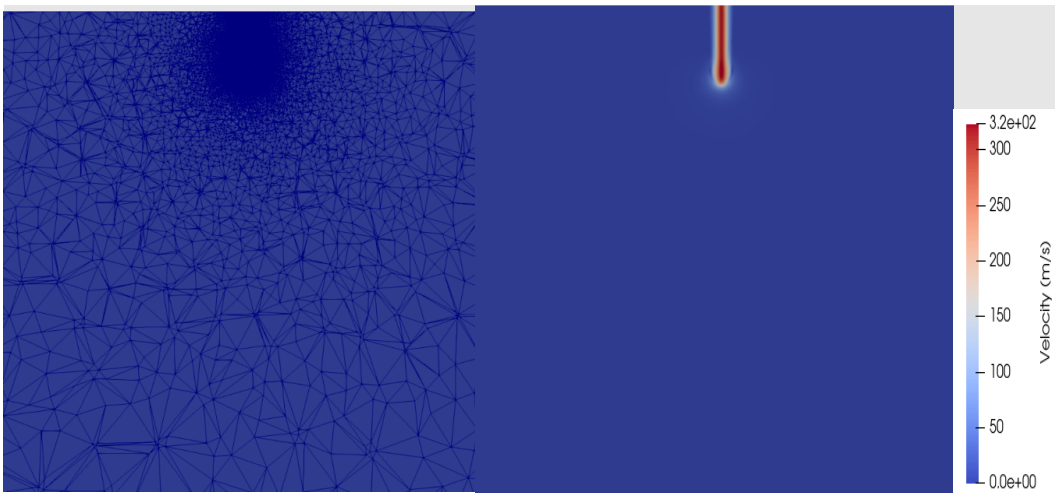

(a) time 100 µs

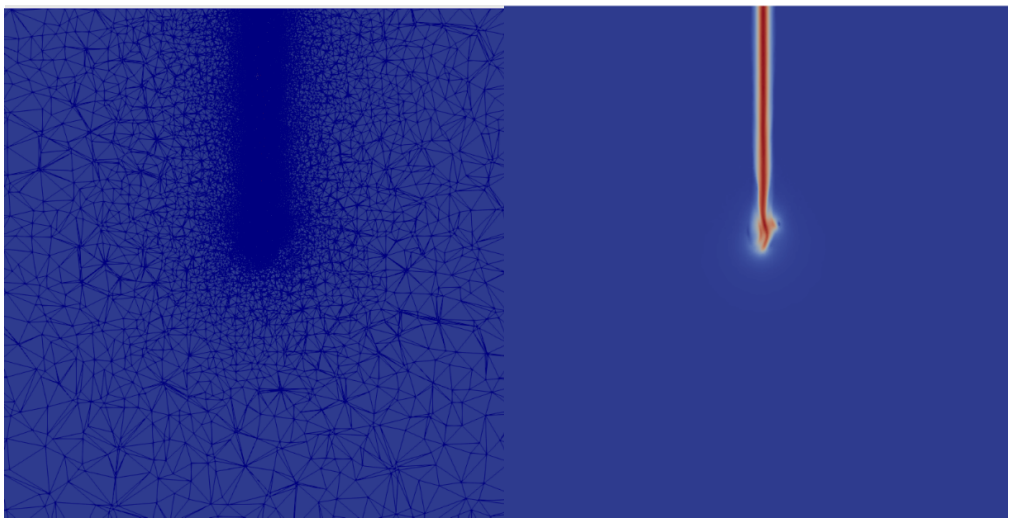

(b) time 200 µs

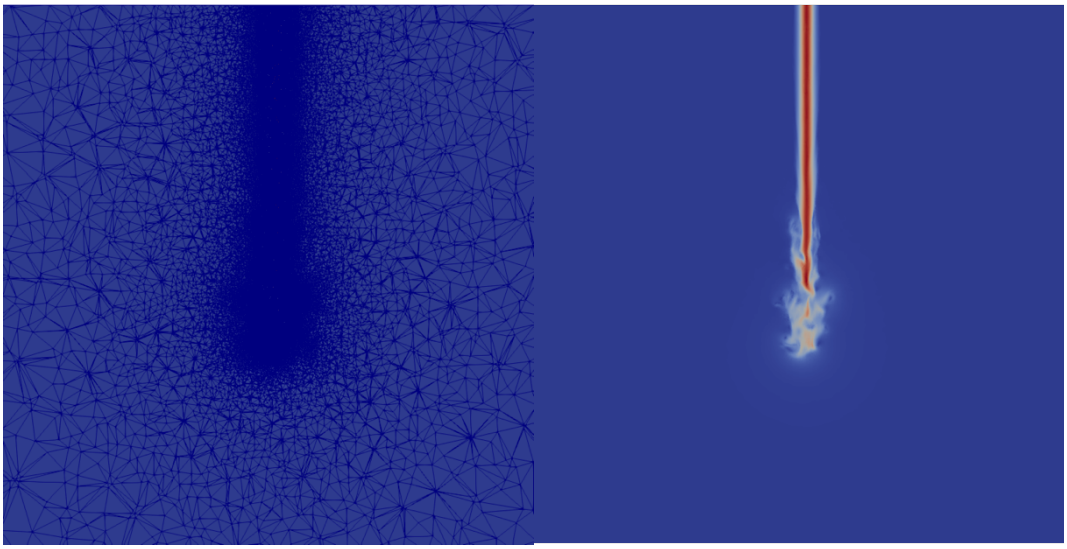

(c) time 300 µs

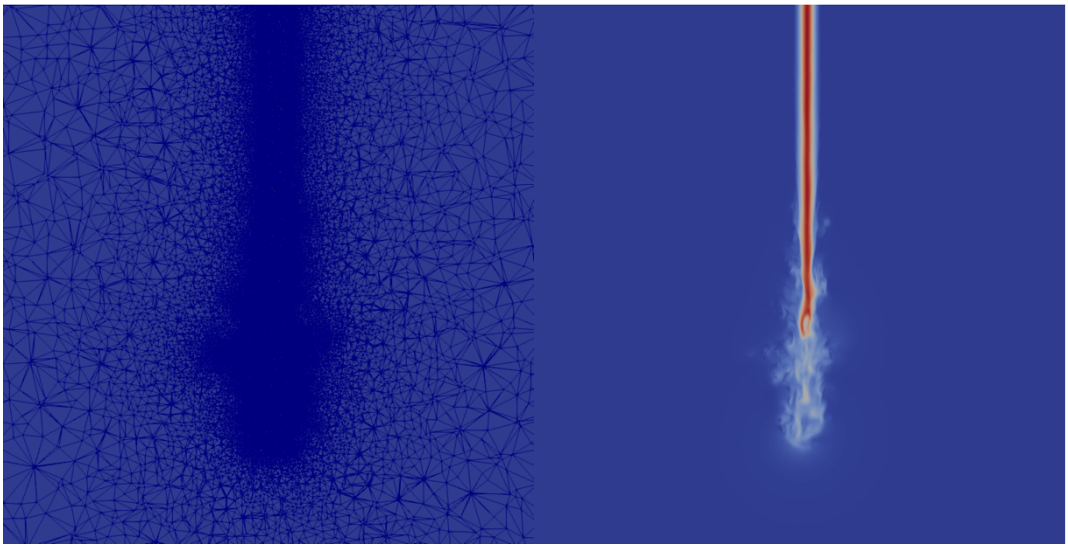

(d) time 440 µs

Figure 21. water jet velocity (right column) and mesh adapting around jet (left column).

Figure 21 demonstrates the simulation of a HPWJ based on an adaptive mesh optimisation which refines the mesh according to the fluid velocity gradient. The minimum mesh edge length is 0.1 mm and the maximum mesh edge length is 5 mm. The fluid mesh used by the IC-FERST code is very refined near the fluid jet and vortices, and relatively coarse elsewhere. Figure 22 shows the fluid axial velocity along the centerline of the jet in contrast to the jet shape (top figure). According to Fig 22, we can divide the jet into three zones: (a) jet axial velocity remains nearly constant 320m/s. In this zone, (H/D ~7) the jet keeps maximum kinetic energy and would generate maximum impinging pressure if it impacts the rock surface; (b) jet axial velocity decreases slightly as small vortices around it affect it. In this zone, jet axial velocity becomes unstable and couldn't maintain maximum impinging pressure; (c) jet axial velocity decreases sharply, and jet turns into more vortices. These results are based on a fully developed profile on entry into the domain.

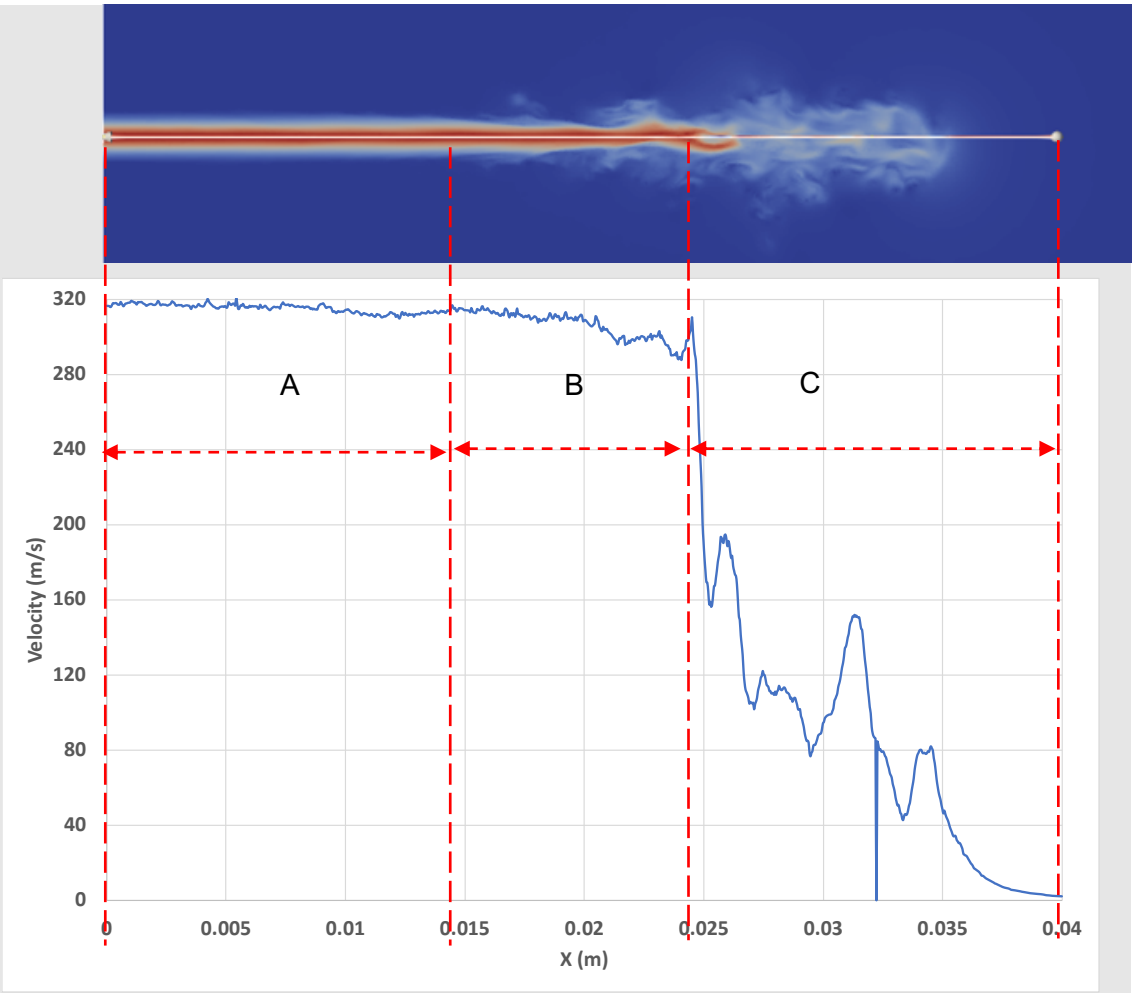

Figure 22. Water axial velocity along the centreline of the jet at time 440 µs.

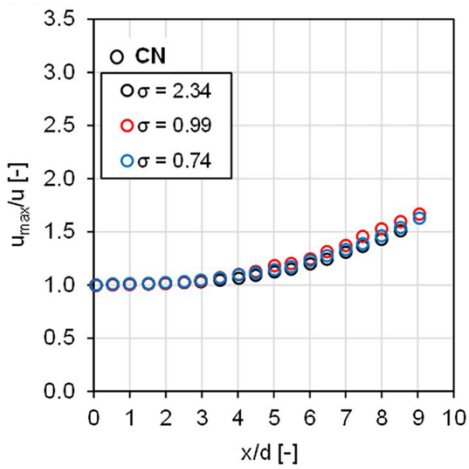

Figure 23. Velocity profile for experiments (from Jasper et al., 2021) where (u_{max}/u) represents the maximum outlet velocity normalised by the centreline velocity.

The conical jet results from Jasper et al. (see **Figure 23**) give the accelerating decline in peak velocity in the jet core with axial distance. With a diameter of 2 mm, the experimental plot shows for the conical nozzle and with no cavitation, after 14 mm (x/d = 7), the centreline velocity has reduced by about 25-30% which is substantially more than in the jet simulated

with IC-FERST. The nozzles in the two cases have different convergence angles and the Re values are different which might explain the discrepancy.

6 Applications

6.1 Domain (A) with Fixed HPWJ

In WP5.1, the main aim is to investigate the effects of HPWJ parameters on impinging pressure, i.e. nozzle diameter, orifice exiting velocity, stand-off distance, and drilling fluids with the additive graphene oxide (GO). We designed a simple fixed jet test. It is important to realise that we are not sampling flows at different distances from the jet outlet with a jet emerging into a large open domain. Here, the domain available for flows is restricted as the stand-off distance is the solid boundary in front of the jet. The domain above the specimen (light blue part in **Figure 25**) is initially filled with fluid with a pressure of zero and has a boundary condition of $p = 0$ at the circumferential and top boundaries (except the red circular area for the fluid jet inflow with the specified velocity profile and the yellow annulus area with a no-slip condition at the top boundary). Our project partner at UPC used their CFD code to simulate the flow in the nozzle with different chamber pressures and they extracted the orifice-exiting velocity distribution in the radial direction (see **Figure 26**). A bi-function is derived to perform curve-fitting (see **Figure 27**) and this was applied at the orifice as a velocity boundary condition and maintained during the simulation once started.

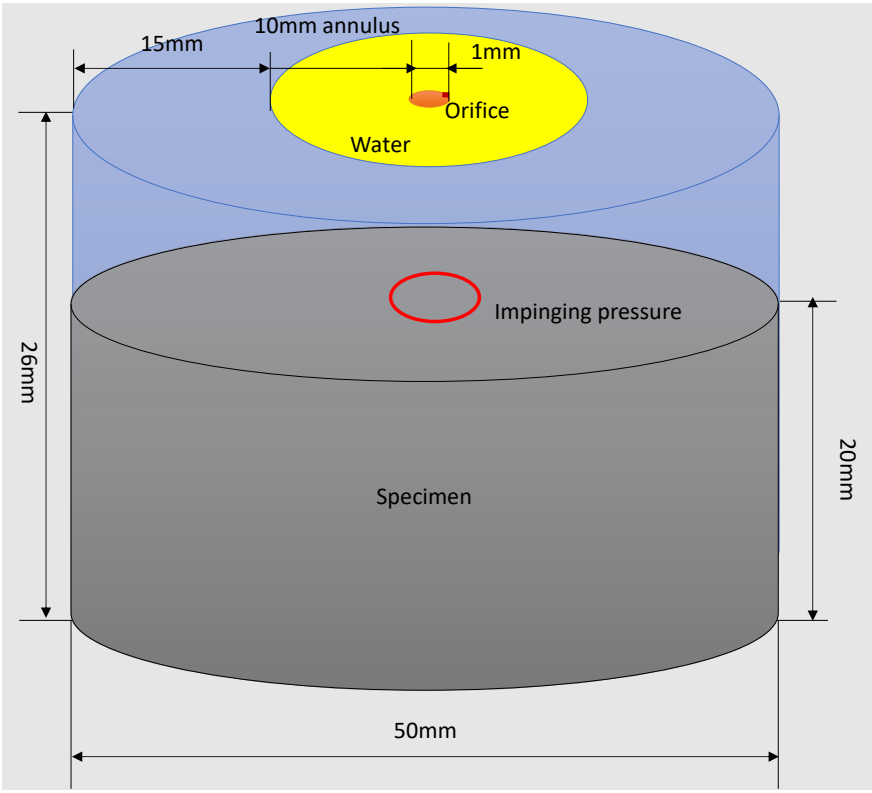

Figure 25. Schematic of simulation setup.

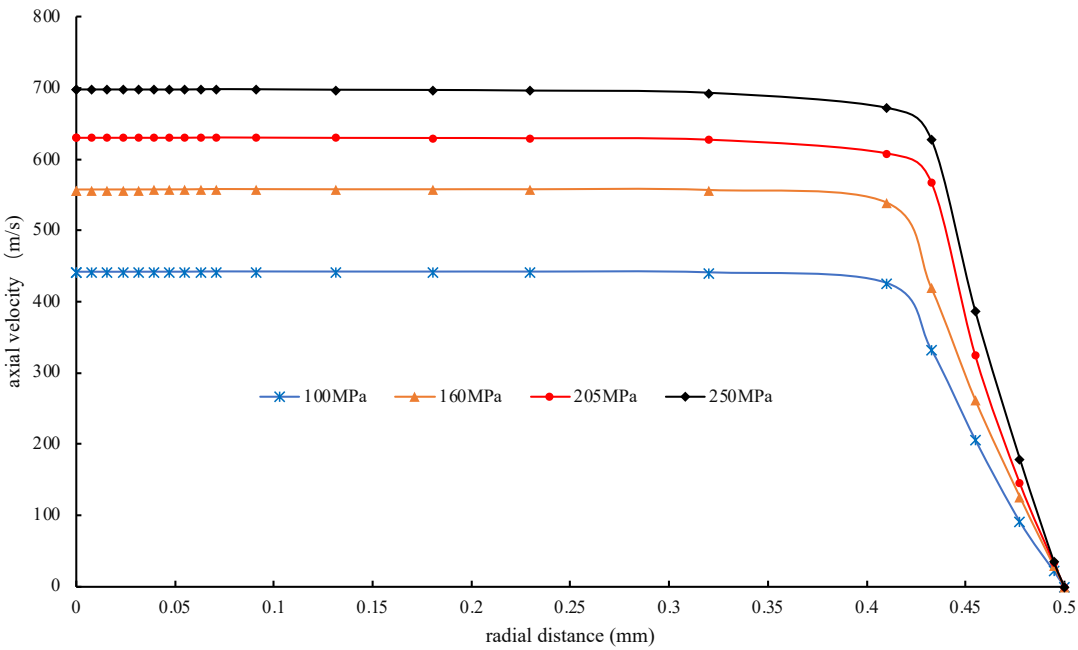

Figure 26. Orifice exiting velocity profile along radial direction as derived from CFD models of UPC (CUP Orchyd Internal Report - “Nozzle simulation results”, July 2021).

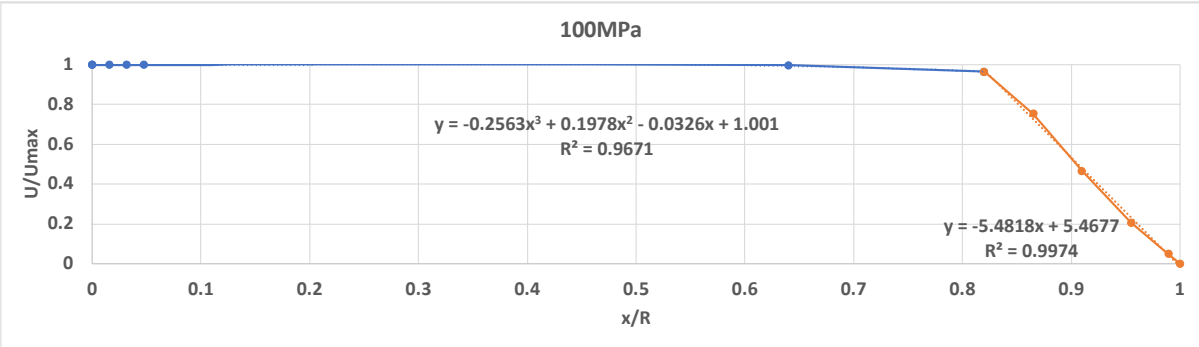

(a) chamber pressure 100 MPa

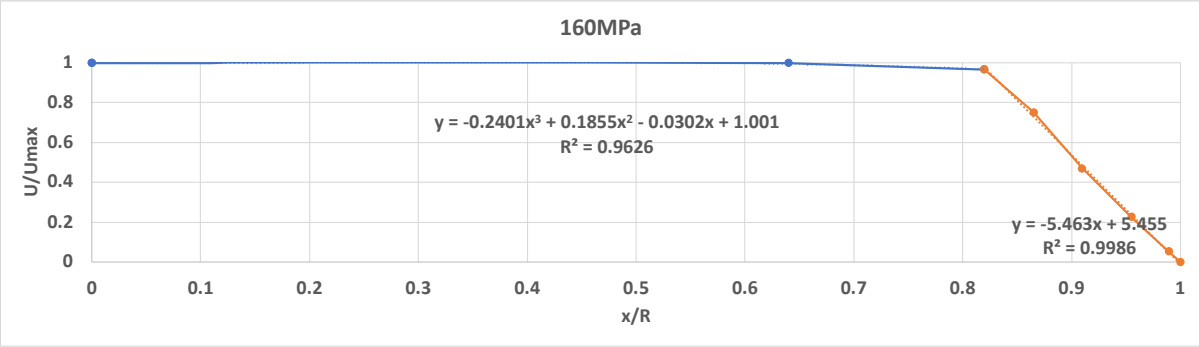

(b) chamber pressure 160 MPa

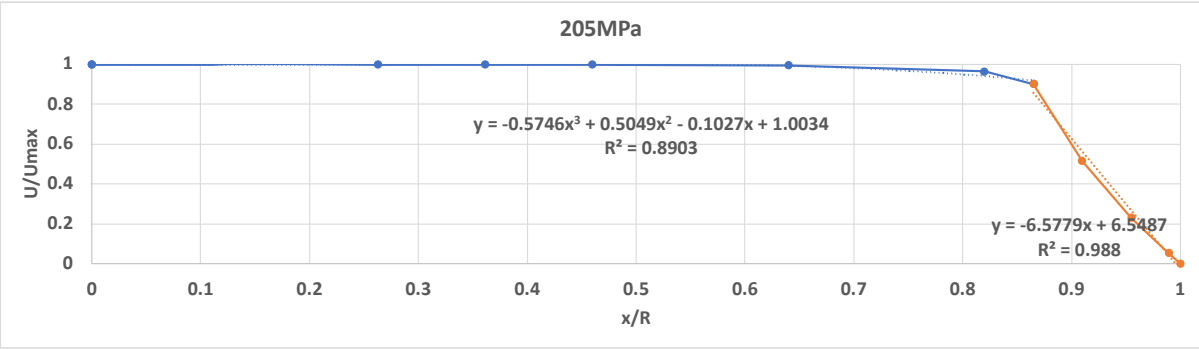

(c) chamber pressure 205 MPa

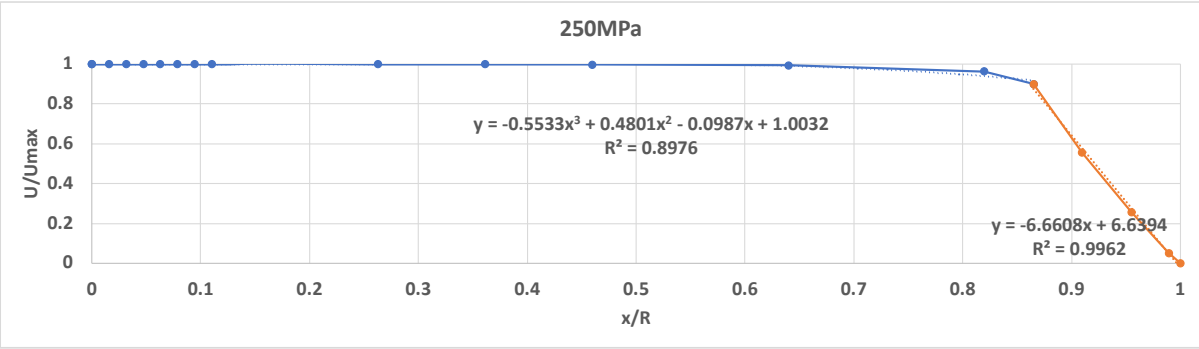

(d) chamber pressure 250 MPa

Figure 27. Profile of fluid velocity at the orifice using bi-function curve-fitting.

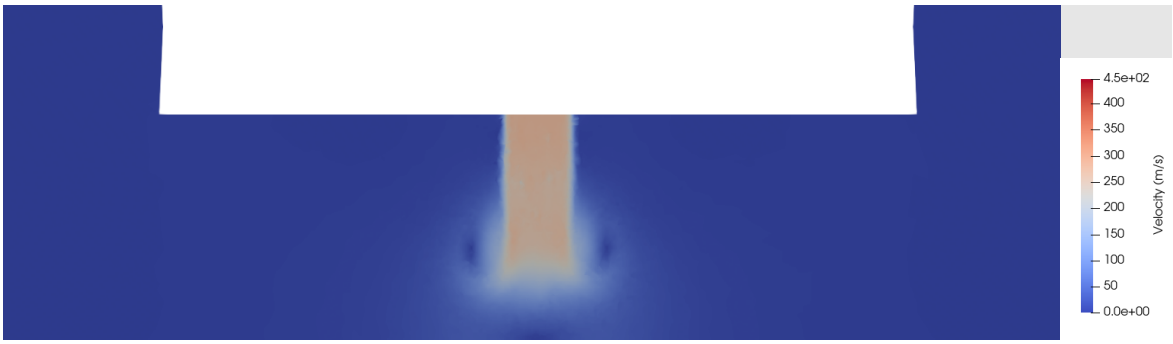

(a) Time 50µs

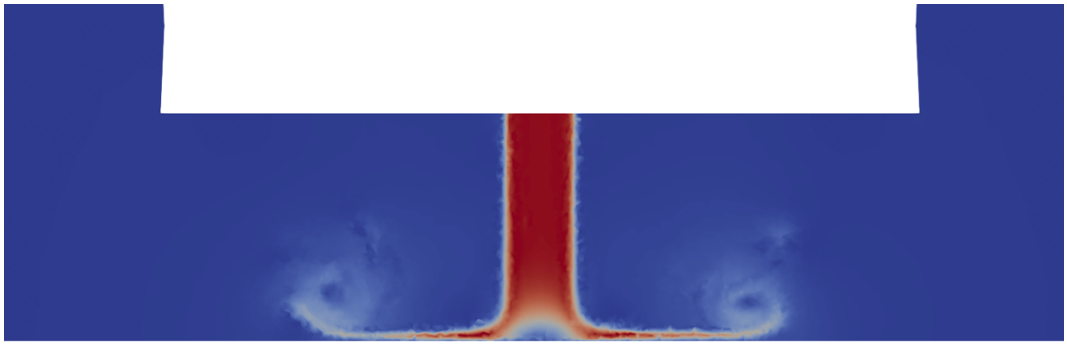

(b) Time 100µs

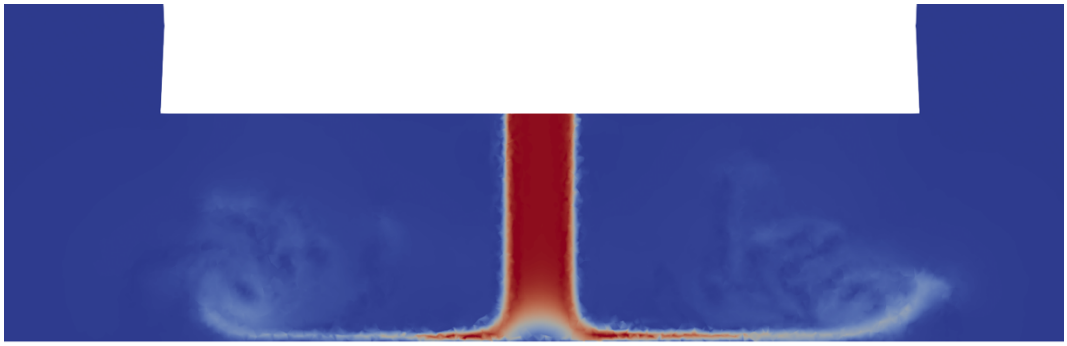

(c) Time 150µs

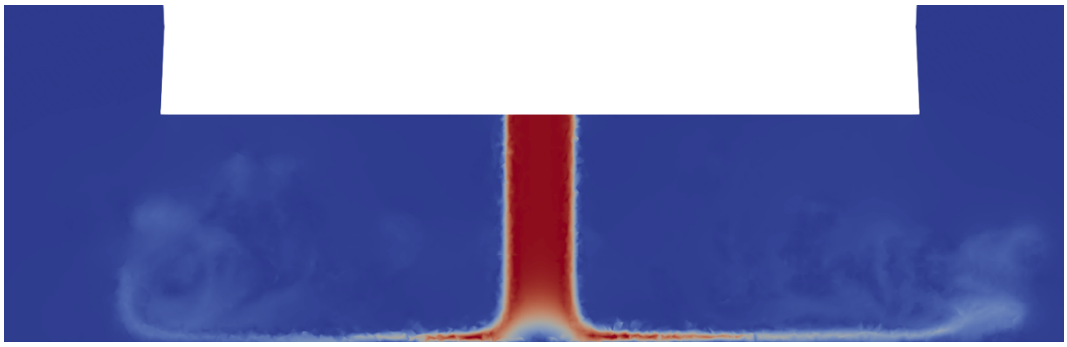

(c) Time 200 µs

Figure 28. Evolution of fluid velocity for HPWJ with nozzle diameter 1 mm, stand-off distance 3 mm and chamber pressure 100 MPa.

(a) Time 50µs

(b) Time 100µs

(c) Time 150µs

(d) Time 200 µs

Figure 29. Evolution of pressure contour in fluid domain for HPWJ with nozzle diameter 1 mm, stand-off distance 3 mm and chamber pressure 100 MPa.

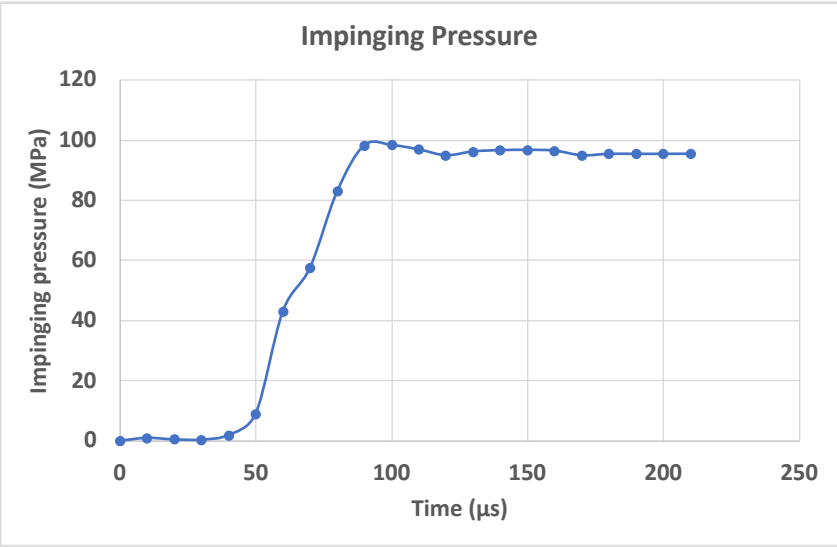

Figure 30. Evolution of impinging pressure for HWPJ with nozzle diameter 1 mm, stand-off distance 3 mm and chamber pressure 100 MP.

Impinging pressure is sampled at the axial point lying on the solid surface boundary using interpolation between nearest neighbour nodes. **Figure 30** Shows the evolution of the jet impacting on the bottom boundary for HPWJ with nozzle diameter 1 mm, stand-off distance 3 mm and chamber pressure 100 MPa. The impinging plate pressure profile has stabilised before t = 200ms. For the chamber pressure 100 MPa, the maximum velocity is 441m/s (see Figure 27a) and the velocity profile in **Figure 27a** is set as velocity boundary condition and ramped up from 0 m/s to 441 m/s linearly within 80µs. After the jet impacts the bottom surface, the impinging pressure overshoots the maximum value of 99 MPa at 90µs and then stabilises to 96.9 MPa (see **Figure 30**).

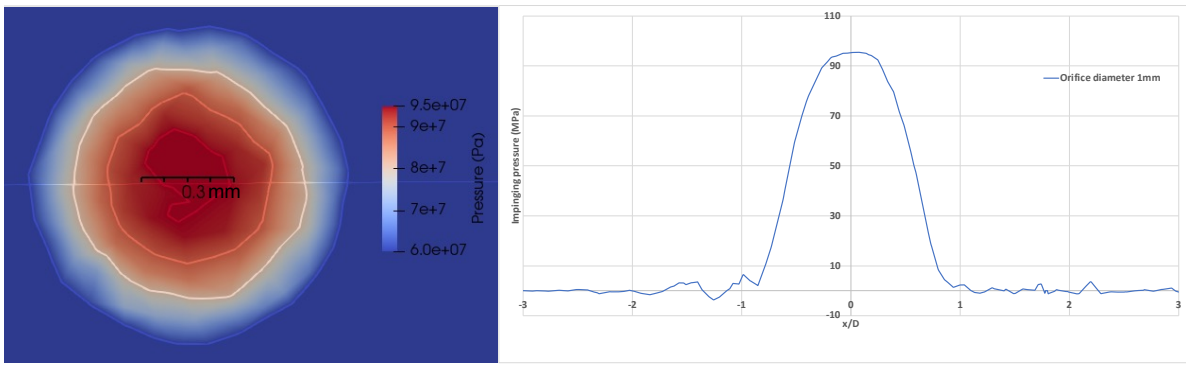

Figure 31. (a) Pressure contours of the impinging bottom surface of jet; (b) pressure distribution along x direction on the bottom surface.

Figure 31 shows the impinging pressure on the impinging plate surface and distribution along x direction. The core pressure contour (arbitrarily plotted here as >95% chamber pressure) is not perfectly circular and symmetric, the width of this >95% zone is about 0.3 mm.

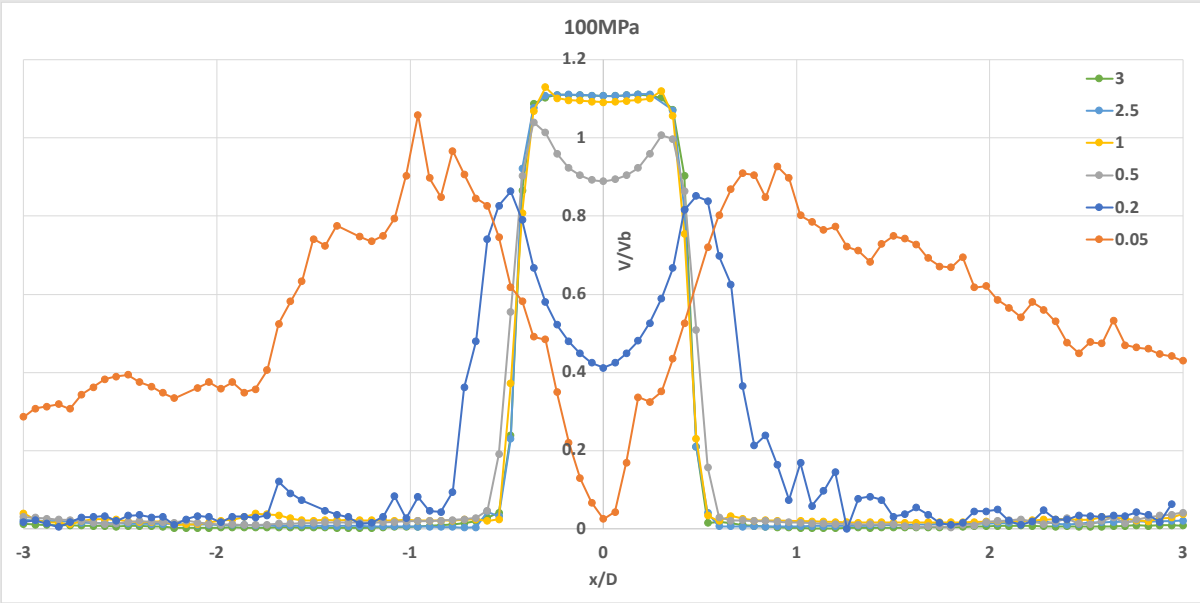

Figure 32. Radial profile development of the normalized mean axial velocity *V*/*V*b at stand-off distance 3 mm (H/D = 3).

Figure 32 shows the distribution of normalised velocity V/Vb along the jet centreline, here Vb is the bulk (i.e., average) velocity through the orifice. Here, we plot horizontal profiles at different distances from the plate (height z=0) up to nozzle at z=3 mm. From the height of z =3D to z=1D, (where D=1 mm) the velocity remains constant in the core region. The velocity in the impinging zone decreases quickly from z=1D to z=0.05D. This agrees with the simulation results published in Wang et al., (2020).

6.2 Effect of chamber pressure on impinging pressure

Table 1 comparison of the numerical results of impinging pressure between ICL and UPC, for the case with stand-off distance = 3D

Chamber pressure	100MPa	160MPa	205MPa	250MPa
ICL numerical results	96.9MPa	155.5MPa	198.5MPa	244.5MPa
UPC numerical results	97MPa	154MPa	198MPa	241MPa

Four numerical tests were carried out for different chamber pressures, 100MPa, 160MPa, 205MPa, and 250 MPa. The corresponding impinging pressures are shown in Table 1. It shows the impinging pressure increases when the chamber pressure increases. We also compared our results with UPC's results. They match each other very well.

6.3 Effect of stand-off distance SD on impinging pressure

We also investigate the effect of stand-off distance on impinging behaviour for a jet with chamber pressure 100 MPa, and nozzle diameter 1 mm. For SD of 3 mm and 6 mm, the impinging pressures quickly converge to an almost constant value (see **Figure 34**). However, for SD 10 mm, the impinging pressure keeps fluctuating as vortices which are generated near

the impinging area affect the velocity field (see **Figure 33**). If we calculate average impinging pressure using the last four points and plot them in **Figure 35**, we can observe the impinging pressure for SD = 3 mm and 6 mm are almost the same but drop to 92.5 MPa for SD 10 mm.

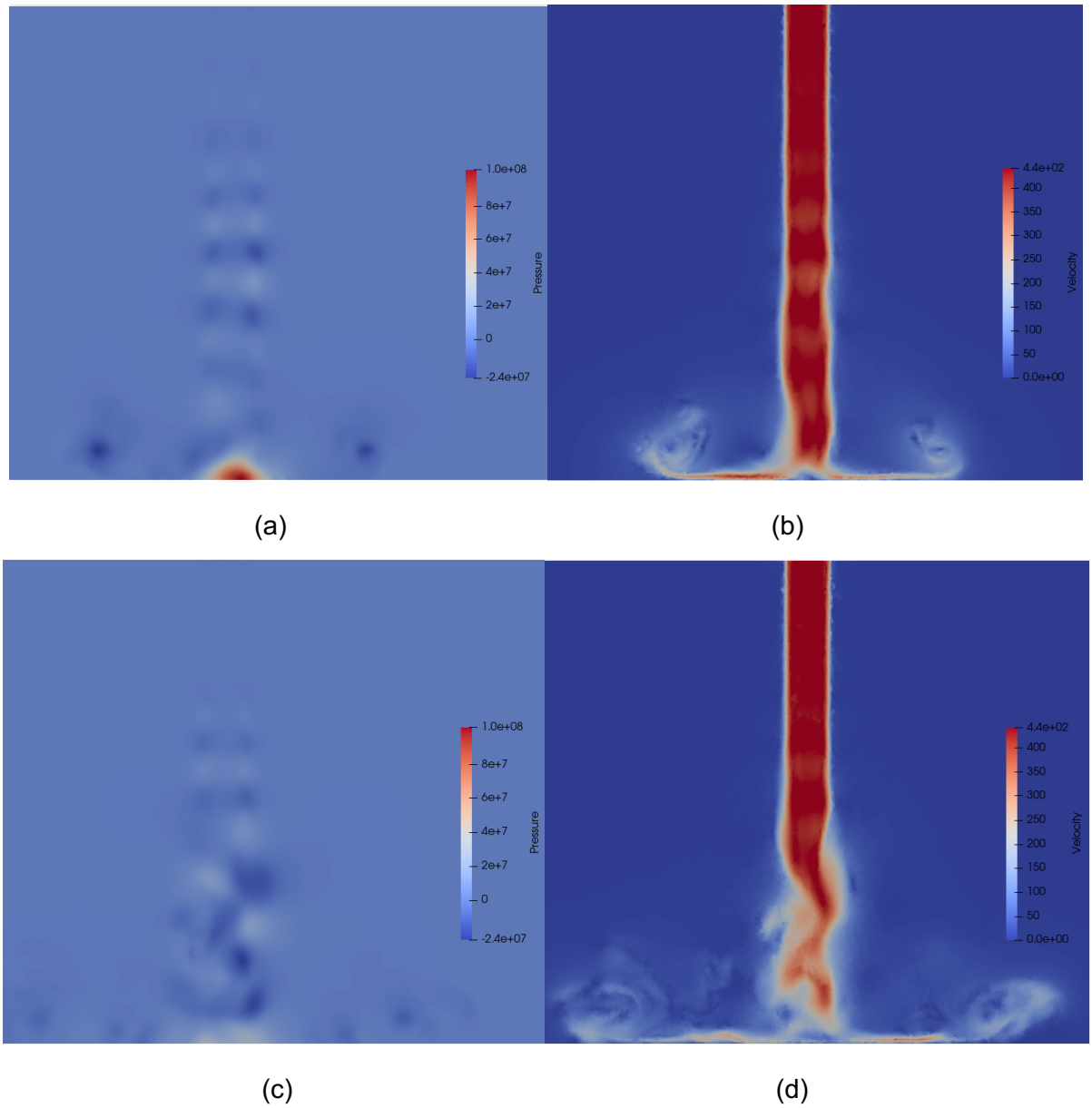

Figure 33. HPWJ with SD 10 mm, chamber pressure 100 MPa, and nozzle diameter 1 mm, pressure distribution at 130 μs (a) and 160 μs (c); velocity distribution at 130 μs (b) and 160 μs (d).

Figure 36 shows the relationship between the imping pressure coefficient and normalised stand-off distance. Compared with the function for the impinging pressure coefficient provided by Wang et al., (2020), our numerical results do not agree with the numerical results published in Wang's paper. This may be because Wang et al. performed simulation under low inlet velocity (0.585-1.76m/s) with wider diameter pipe (20 mm) and Reynolds number (11,700-35,100). We aim to simulate a high pressure and velocity water jet with inlet velocity (320 to 706 m/s) and a higher Reynolds number (320,000 to 706,000). It is worth pointing out that our results match UPC's results very well. In future, we may design and perform more tests under lower Reynolds number.

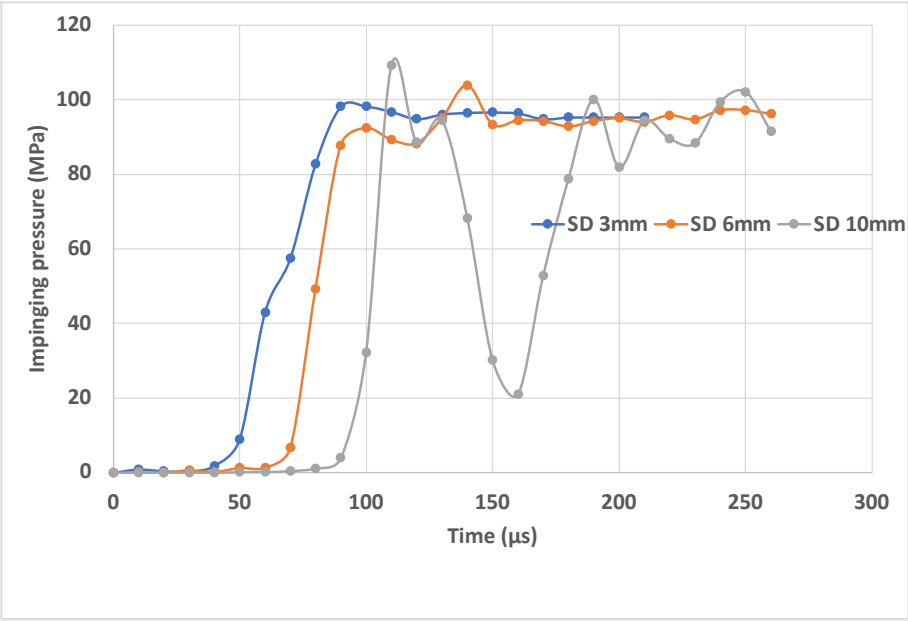

Figure 34. Evolution of impinging pressure for SD 3mm, 6mm, and 10mm.

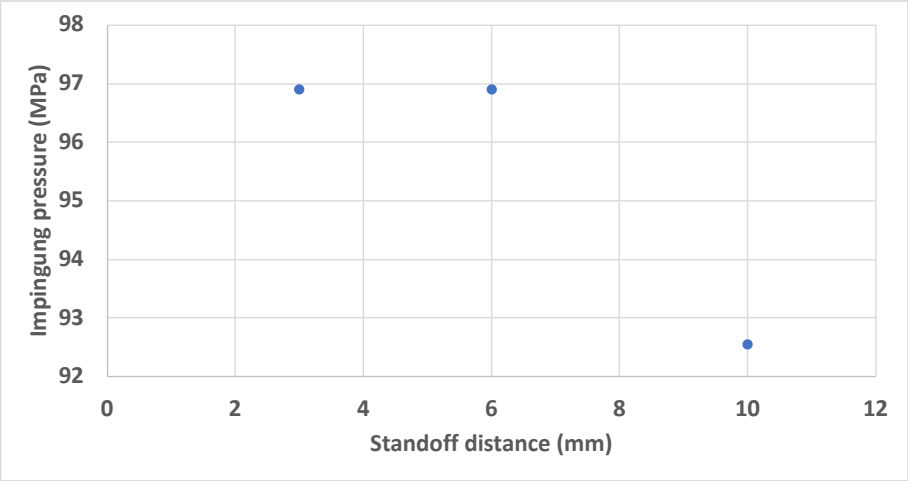

Figure 35. Average impinging pressure for different SD 3mm, 6mm, and 10mm.

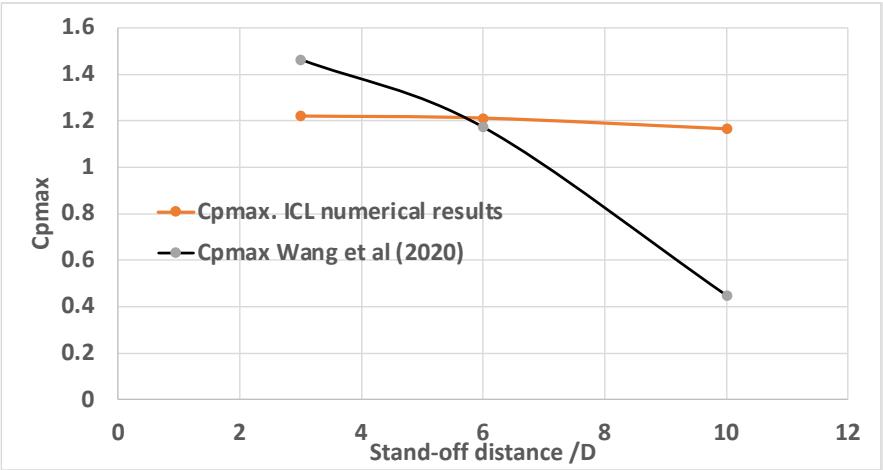

Figure 36. Relationship between C_{pmax} and normalised stand-off distance.

6.4 Effect of nozzle diameter

6.4.1 Constant Chamber Pressure Case

Diameter of the nozzle is a significant factor which affects the impinging behaviour of the jet. To investigate this effect, we choose three diameters of the nozzle, 1 mm, 0.8 mm, and 0.5 mm for the jet with calculated velocity distribution associated with chamber pressure of 100 MPa by UPC and SD 3 mm. In the work reported here in Section 6.4, first, the same chamber pressures and therefore the same velocity distributions (as a function of normalised diameter) are considered for each of the three nozzle diameters. The three different nozzle orifice diameters lead to three different discharge volumetric flow rates and therefore different pump power. **Figure 37** shows impinging pressures for the three orifice diameters all converge to a similar maximum value ~97 MPa. But for diameter 0.5 mm, it becomes more unstable and fluctuates more widely. **Figure 38** shows the impinging pressure on the impinging surface and the distribution in the radial (x) direction for orifice diameter 0.8 mm and 0.5 mm. It is notable that the core impinging pressure contours (>95% chamber pressure) are not circular and symmetric, the width of this core zone decreases from 0.3 mm to 0.1 mm when the orifice diameter decreases from 1 mm to 0.5 mm (compare **Figure 31** and **Figure 38**). **Figure 39** shows the impinging pressure distribution along the x direction for orifice diameter 1 mm, 0.8 mm and 0.5 mm. The maximum values for the three orifices are almost the same, but the core impinging pressure zone becomes narrower when the orifice diameter decreases from 1 mm to 0.5 mm. Further investigation is required to explore the effect on inlet velocity of a reduced nozzle diameter for the same power e.g., as delivered by the intensifier.

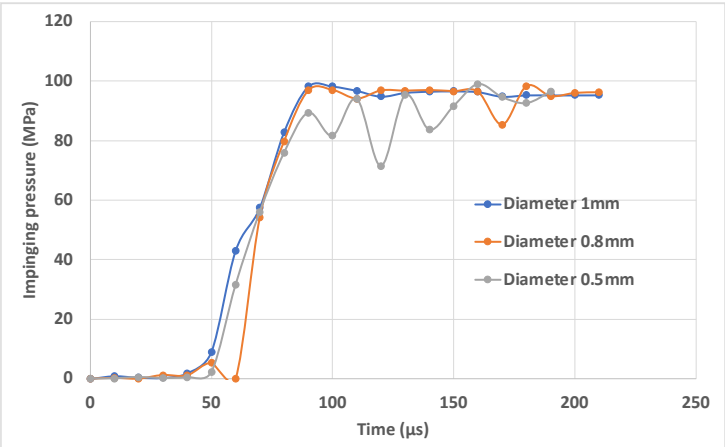

Figure 37. Evolution of impinging pressure for nozzle diameter 1 mm, 0.8 mm and 0.5 mm.

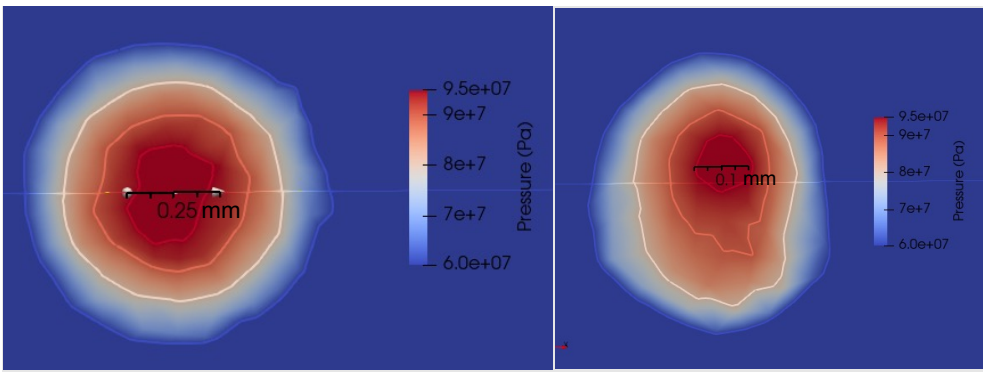

Figure 38. Pressure contours for constant pressure case. Left: 0.8 mm, Right: 0.5 mm.

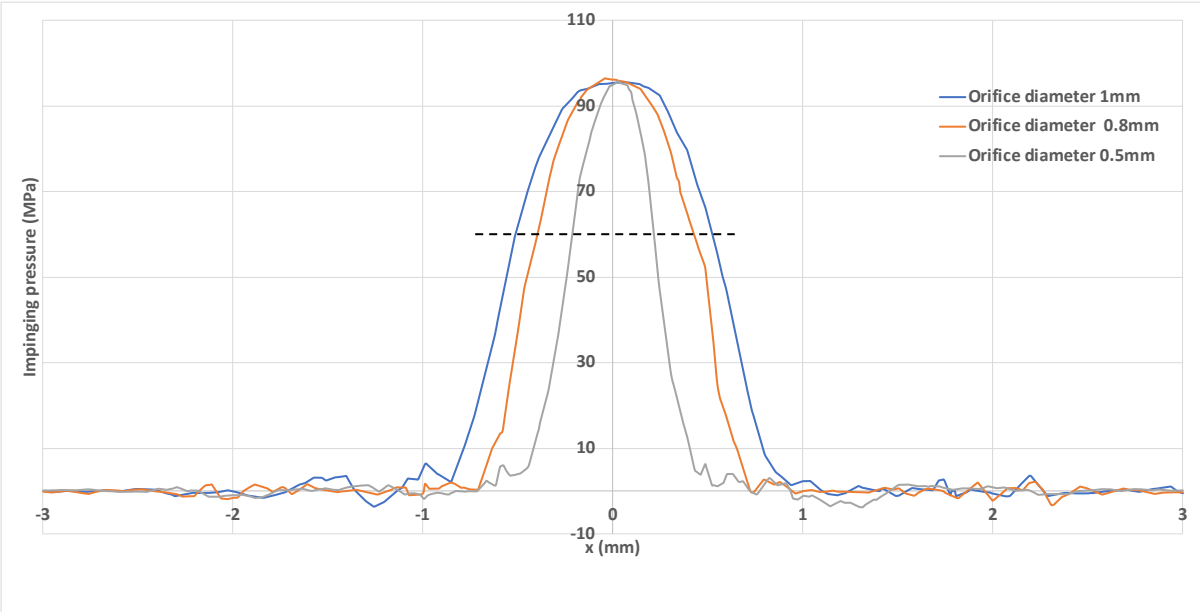

Figure 39. Pressure distribution along the x direction on the bottom impinging plate surface.

6.4.2 Constant Power Case

In this section, to further investigate the effect of nozzle diameter, we choose two diameters of the nozzle, 1 mm, and 0.8 mm but here each jet is created with same pump power. For the 1 mm nozzle, we use the same condition described in Section 6.1, i.e., a chamber pressure of 100 MPa, and the appropriate velocity distribution associated with chamber pressure of 100 MPa determined by UPC. This average velocity is 398.6 m/s, and we again consider the impinging pressure for SD of 3 mm. Using Data supplied from Karcher nozzle technical manual, we calculate the pump power as 31.31 kw for this jet. To use the same pump power for the 0.8 mm nozzle, we calculated the chamber pressure to be 130 MPa, and the average velocity, 464 m/s. Now we know that from considering UPC results in **Figure 26** that the flat top distribution is slightly broader for higher pressure flows, but this is not a very significant effect, so for simplicity, the normalised velocity distributions with respect to the diameter are assumed the same for the two nozzles. **Figure 41** shows the impinging pressure distributions acting radially and along the x direction for orifice diameters of 0.8 mm and 1 mm. The maximum impinging pressure for 0.8 mm and 1 mm are about 127 MPa and 97 MPa respectively. The impinging pressure distribution becomes narrower when the orifice diameter decreases from 1 mm to 0.8 mm (see **Figures 40** and **41**). As the 0.8 mm nozzle produces a much higher maximum impinging pressure, it will have generated more destructive power when the jet impacts the rock.

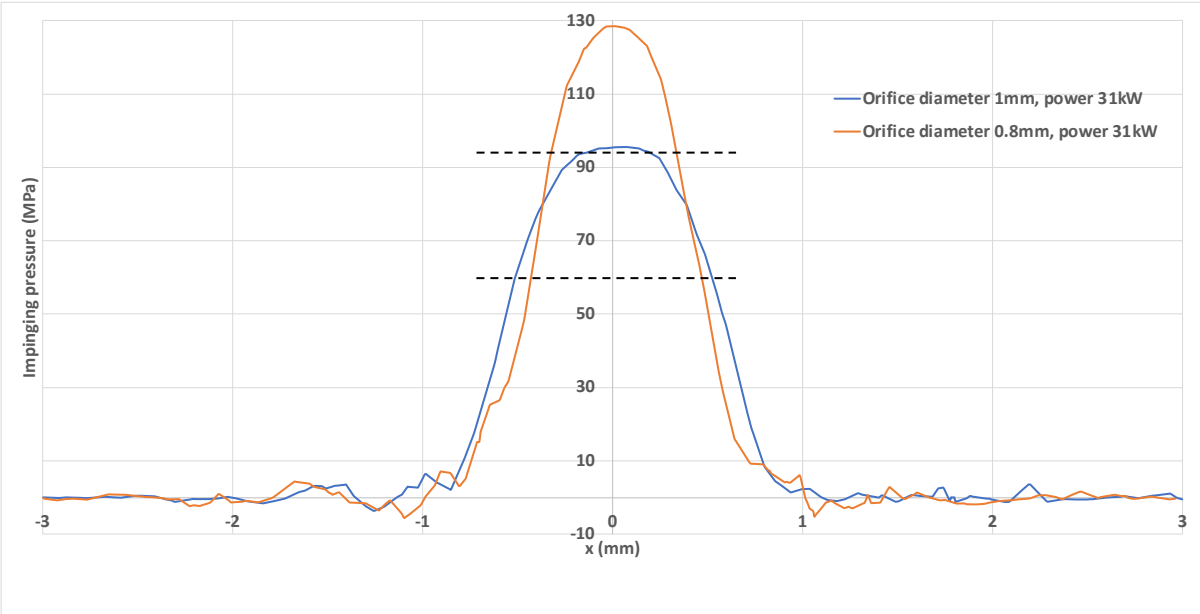

Figure 40. Pressure distribution along the x direction on the bottom impinging plate surface, highlighting 60 MPa and 95 MPa contours.

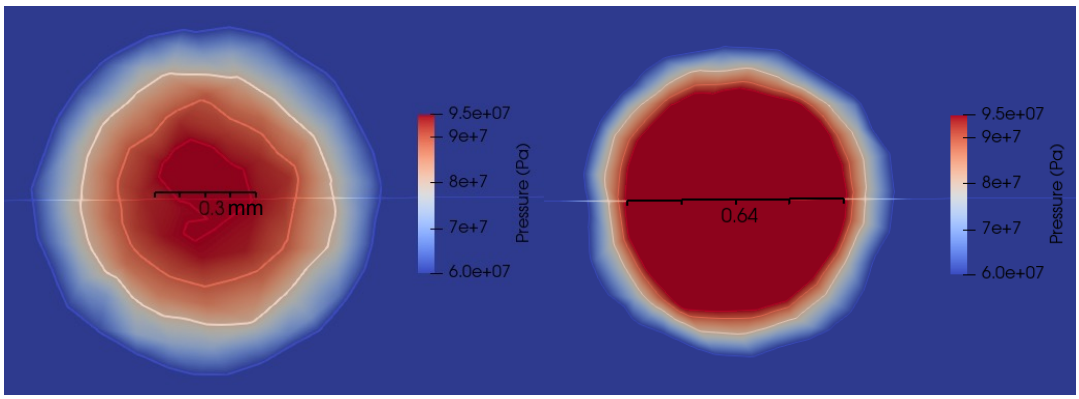

Figure 41. Impinging pressure contours highlighting 95 MPa (red) and 60 MPa (blue) for constant pump (or intensifier) power case, Left: diameter = 1.0 mm, Right: diameter = 0.8 mm, for same stand-off distance SD = 3 mm.

These simulations suggest that if equal power is available from the intensifier with a slightly smaller diameter nozzle orifice, that a slightly smaller area on the impinging plate is exposed to pressures of 60 MPa. But if we were to set a hypothetical threshold pressure level for which rock damage starts to become appreciable at say, 95 MPa, the area suffering damage is at least 4 times greater for the 0.8 mm diameter jet. If that threshold were set precisely at say, 120 MPa, only the 0.8 mm diameter jet would generate any rock destruction and for this theoretical case the damage zone would be about 0.4 mm wide. None of this hypothetical discussion takes account of any real rock grain structure, but it does illustrate the trends expected and the potential to model the potentially most advantageous diameter for a given power and stand-off distance.

6.5 Effect of non-Newtonian fluids

6.5.1 Viscometer Data

For Newtonian fluids, viscosity is independent of shear rate. For example, water's viscosity remains constant for a constant temperature, 1 mPa.s at 20 °C. But there are many non-Newtonian fluids which show different behaviour, e.g., in drilling fluids with additive, the viscosity at low shear rates is significantly higher than for water but decreases when shear rate is higher (see **Figure 42**).

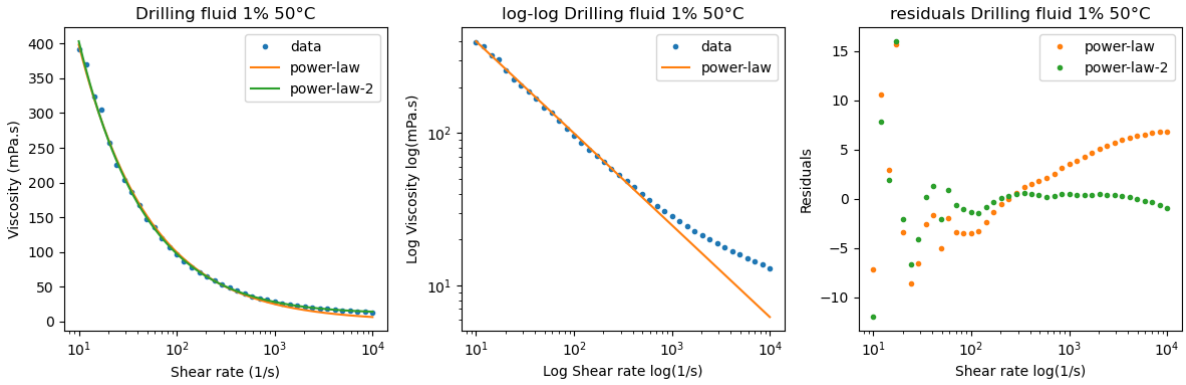

Figure 42. Effective viscosity vs shear rate (blue dot line) and approximation by power law (orange line) and double power law (green line) (provided by Sintef).

6.5.2 Curve-fitting model

In the ORCHYD project, to increase the stability of the wellbore during geothermal well drilling, graphene oxide was chosen as additive to drilling fluids. Our project partner Sintef measured the viscosity for base fluids of water and drilling fluids with different additive concentration (0%, 0.1%,0.35% and 1%) over a range of shear rates. To analyse the relationship between viscosity and shear rate, single and double power laws were prepared by Sintef (see **Figure 42**). The double power law was chosen and modified after experimental raw data were further analysed. To demonstrate the effect of non-Newtonian fluids, we selected an experimental data set of drilling fluids at 50ºC, with 0%, 0.1%, 0.35% and 1% additives and compared them with pure water at 20 ºC which is a Newtonian fluid. After analysing the experimental data provided by Sintef, we found that the experimental data is measured over a narrower range (1 to 10^4) of shear rate than observed in numerical simulation results (1 to 10^6). We need to extrapolate experimental data for shear rate from 10^4 to 10^6. After carefully analysing the raw data, we also found that measured viscosities of Drilling fluid with additive 0%, 0.1%, and 0.35% appear to have converged to constant values of 2.72 mPa s, 3.5 mPa s, and 5.7 mPa s respectively at shear rate 10^4 s^{-1} (see **Figure 43**). This suggests we can use cut-off values at shear rate 10^4 s^{-1} to extrapolate the experimental data from 10^4 to 10^6 for shear rate (see **Figure 43a-c**). But for drilling fluid with additive 1%, **Figure 43d** shows the experimental data has not reached constant value at shear rate 10^4 s^{-1}. We performed a regression analysis to estimate the relationship between minimum viscosity and additive concentration (see Figure 44). We estimate the minimum viscosity of drilling fluid with additive 1% is about 13.09 mPa s. If we use the double power law formula drilling fluid with additive 1% in **Figure 45d**, the minimum viscosity is 12.98 mPa s.

To investigate the effect of non-Newtonian fluid, the same setup and boundary conditions described in Section 6.1 are used. For inlet velocity profile, we used the velocity distribution

for chamber pressure of 100 MPa presented in **Figure 27a**. Five fluids were selected to address the objectives of assessing a range of fluids, i.e., drilling fluids at 50ºC, with 0%, 0.1%, 0.35% and 1% additives and pure water at 20 ºC. We also carried out simulations using three stand-off distances, 3 mm, 6 mm, and 10 mm. The numerical results of the evolution impinging pressure are shown in **Figures 46-48**. Based on these results, we can conclude that impinging pressure is not sensitive to the viscosity changes. This maybe because the HPWJ is an inertia-dominated system, and that impinging pressure is not sensitive to Reynolds number changes resulting from small changes in viscosity.

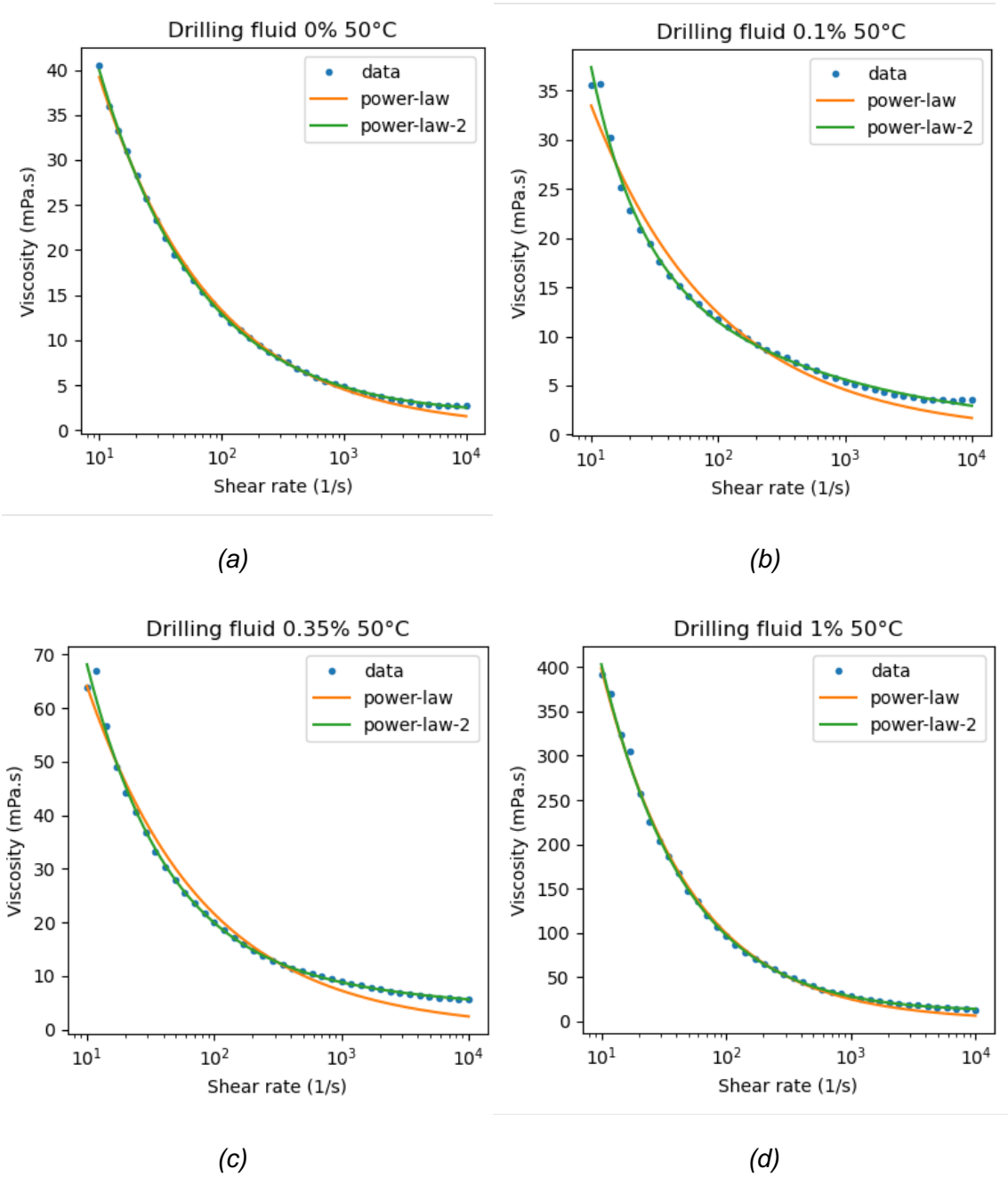

Figure 43. Viscosity vs shear rate for drilling fluids with additive concentrations (a) 0%; (b) 0.1%; (c) 0.35%; (d) 1%.

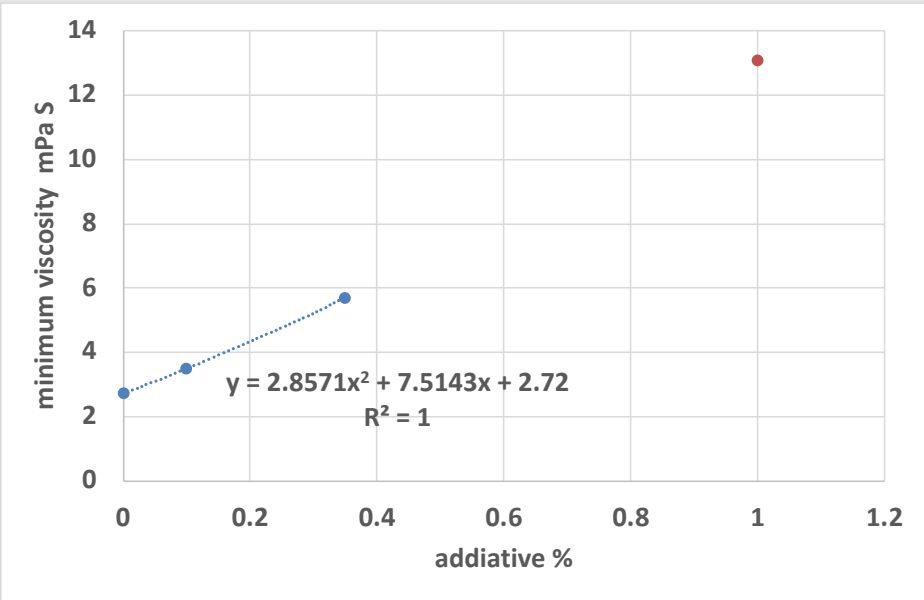

Figure 44. Correlation between minimum viscosity and additive concentration and an extrapolation data point.

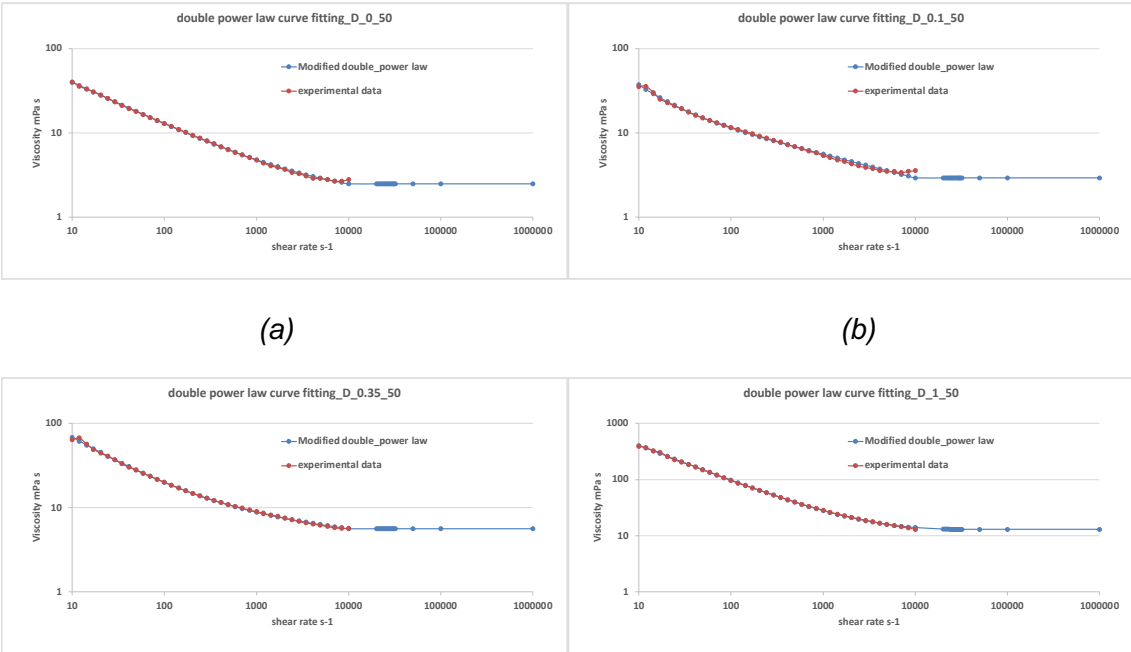

(a) *(b)*

(c) *(d)*

Figure 45. Curve-fitting and extrapolating of experimental data for (a) drilling fluid without additives; (b) drilling fluid with 0.1% additives; (c) drilling fluid with 0.35% additives; (d) drilling fluid with 1% additives.

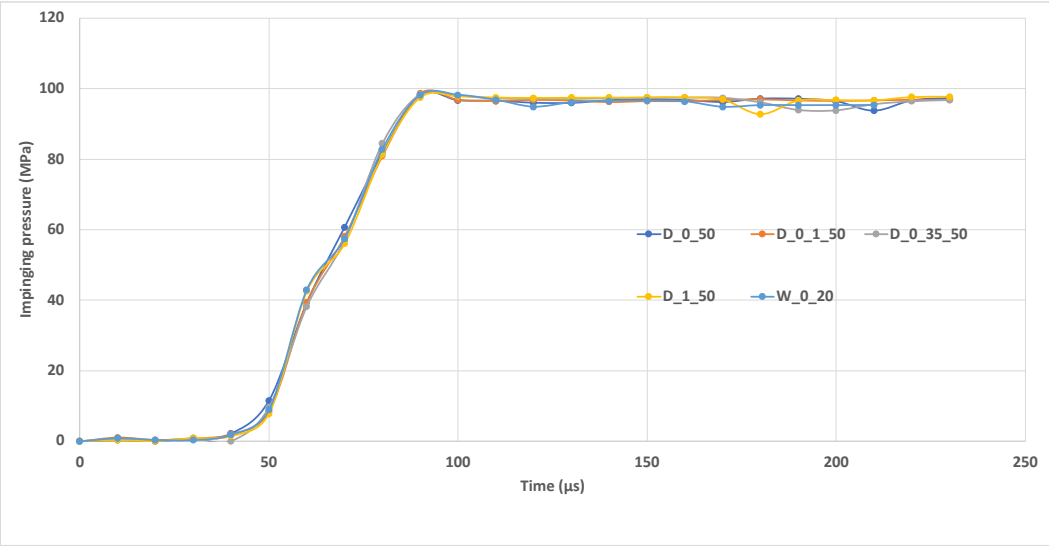

Figure 46. Evolution of impinging pressure for SD of 3 mm.

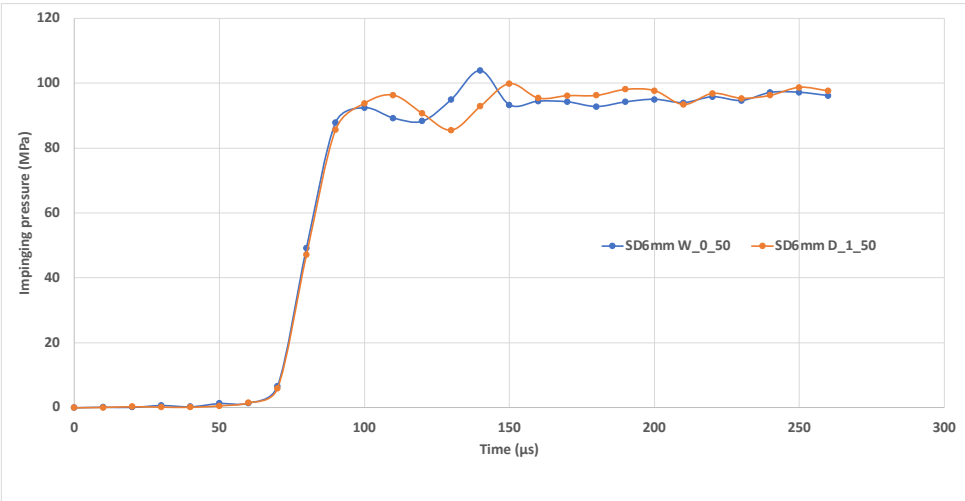

Figure 47. Evolution of impinging pressure for SD of 6mm.

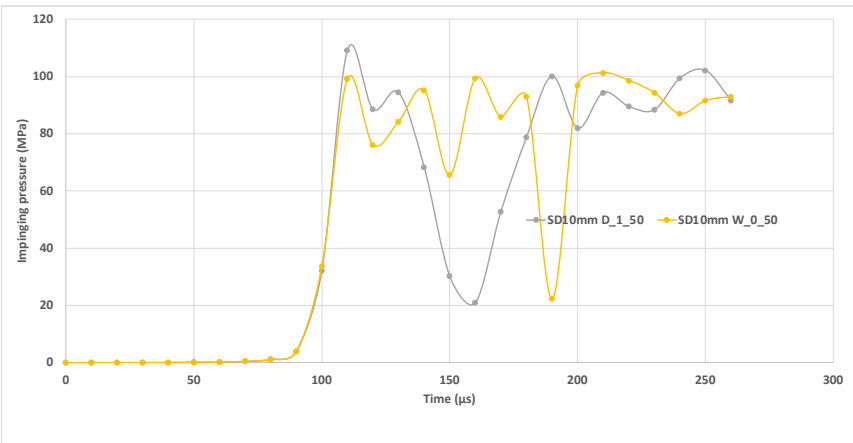

Figure 48. Evolution of impinging pressure for SD of 10mm.

6.6 Rotating nozzle simulation for Laboratory Rig - Domain (B)

For rotational nozzles, the rotating speed may influence the behaviour of the jet and jettability of jock. To improve the ability to optimise the set up for improved jettability under the action of a rotating jet, we also designed a simple rotating jet test in WP5.1. The domain (see **Figure 49**) is initially filled with fluid with a pressure of zero and has a boundary condition of $p = 0$ at the circumferential and top boundaries (except the red circular area for the fluid jet inflow with the specified velocity profile and the blue annulus area with a no-slip condition at the top boundary).

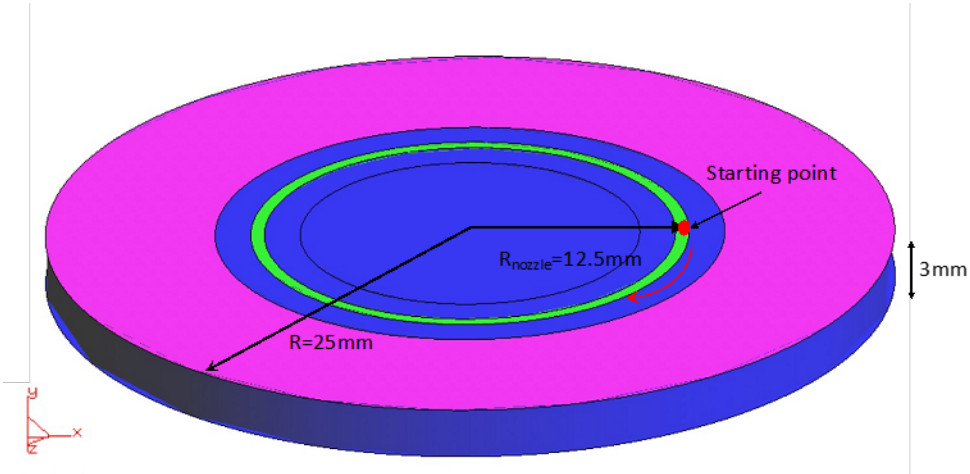

Figure 49. Schematic of simulation setup.

The code, IC-FERST, allows users to insert user-defined functions with time via Python script. We developed a piece of Python script to implement equations (6)-(13) to calculate inlet velocity with time. The code is attached in the appendix. **Figure 50** presents a water velocity vector plot around the jet and impinging pressure on bottom surface at different times. If we select two points (Point A. 0.012401434, 0.0, 0.001566665; Point B. 0.012278591, 0.0, 0.002342266) in the impinging zone along the path of the nozzle and plot the impinging pressure in **Figure 51**, we can see two very similar pressure pulse signals appear one after another, point B lags 500 μs behind point A.

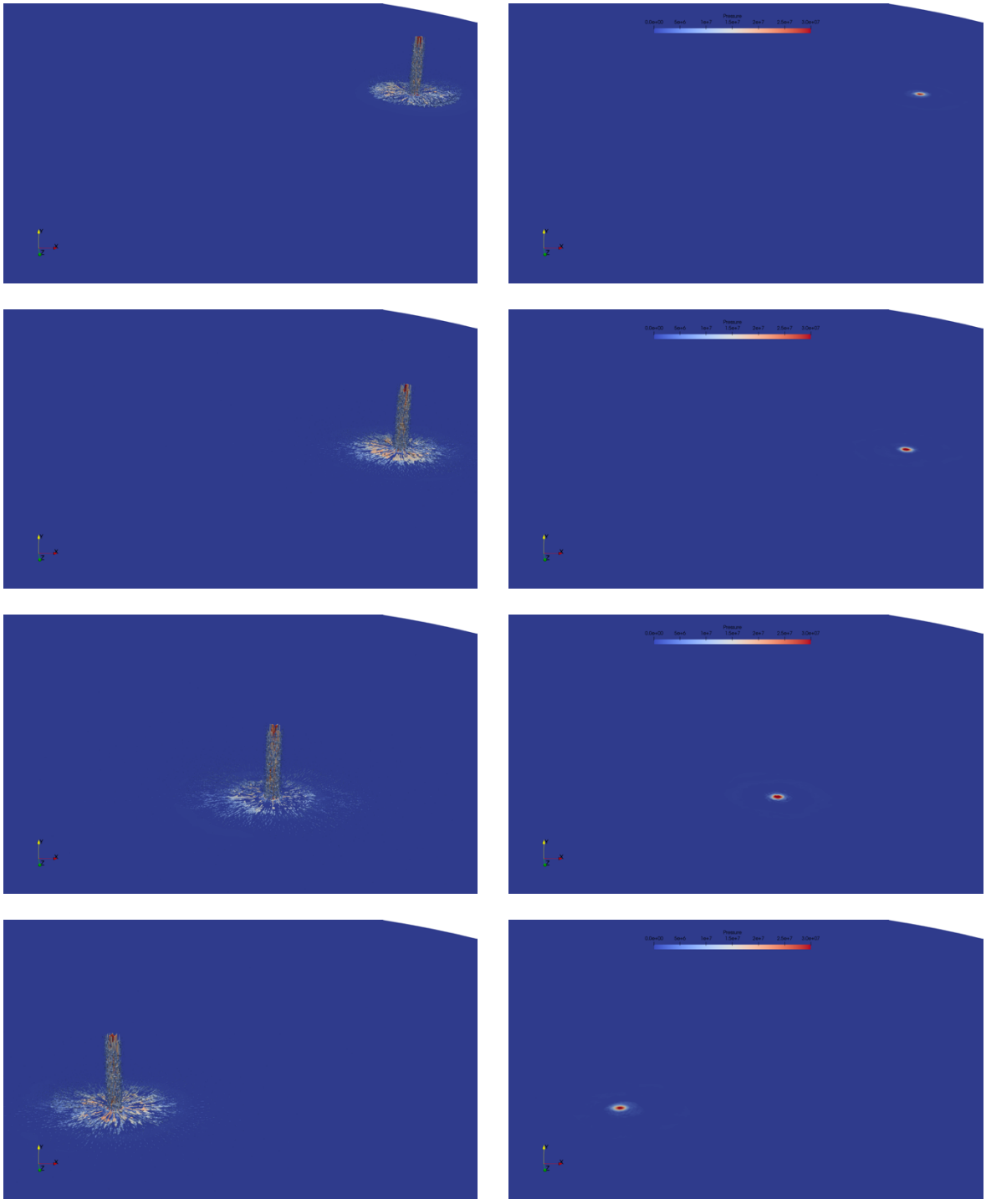

Figure 50. Visualisation of 3D results of the progressive rotating traverse of the jet acting on the base of the domain at the following times (top to bottom): 0.2 ms, 5 ms, 10 ms, 14 ms; left: velocity vector plot, right: impinging pressure on bottom surface.

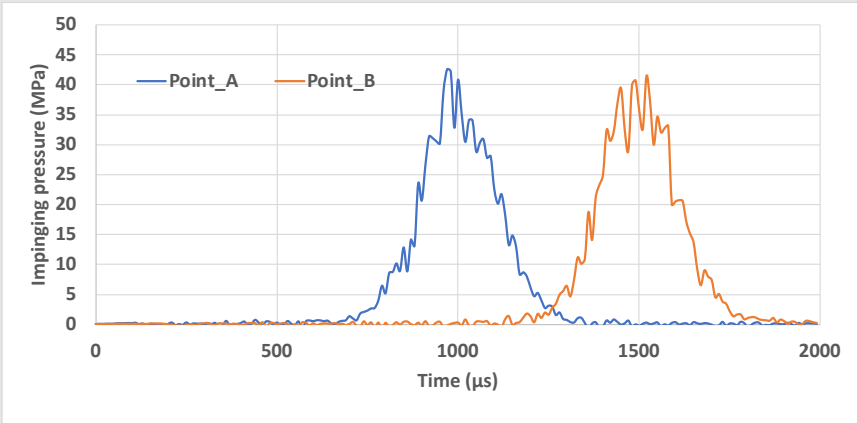

Figure 51. The evolution of impinging pressure at point A and B that lie on the path of a rotating jet traversing on a circular trajectory mimicking the rotating bit.

7 Discussion and Conclusions

Here, we recall the task objectives:

(i) to implement modifications to IC-FERST for non-Newtonian jetting fluid rheology

(ii) to implement modifications to IC-FERST for a rotating reference frame of the nozzle with respect to the solid

(iii) to validate the new IC-FERST model of HPWJ through a comparison with available literature

(iv) to examine the effect on flow and impinging pressures of a range of nozzle orifice diameter, stand-off distance and nozzle chamber pressures for the base case of water, and also the extremes in drilling fluid rheology considered in ORCHYD.

First, to prepare for the new application, we implemented a generalised non-Newtonian fluid law into IC-FERST and the rotating nozzle as a velocity boundary condition over time through a Python script (see Appendix) and demonstrated the capability of code to simulate the rotating nozzle, i.e., objectives (i) and (ii).

Second, to respond to objective (iii) we compare results of the CFD code, IC-FERST using a long and wide domain test described in Section 5. The results qualitatively match published experimental results (Jasper, et al., 2020). For this nearly infinite domain, the jet keeps maximum kinetic energy in the core zone (H/D from 0 to 7). The jet axial velocity notably reduces when H/D is greater than 7. Therefore, in practice the new results for a long wide domain would suggest the stand-off distance should be smaller than 7D to maximise jet energy. As Jasper et al. only carried out the experiments under lower Reynolds number (163,000–180,000) and with a different nozzle, so to compare with our numerical tests (Re: 320000-700000), we need to validate our model further. Fortunately, our project partner, ARMINES, will design and carry out experiments with an impinging plate pressure sensor system and for high Re, and with the same nozzle geometry that we are using in these simulations. In future, we will compare our numerical results with theirs. If we take the impinging surface into account in defining the domain geometry, the impinging pressure values for each stand-off distance will differ from those suggested by an infinite domain, because the

flows are different. Interestingly, for the case H=10D, the largest domain, our results agreed closely with UPC's results.

Third, addressing objective (iv) we investigated the effect of the chamber pressure on impinging pressure. We found the impinging pressure increases when the chamber pressure increases. UPC also carried out the same simulation setup with different code and using the same chamber pressures. We compared our results with UPC's results (see Table 1) and found there was a very close agreement.

Fourth, also addressing objective (iv) we investigated the effect of the stand-off distance on impinging pressure for jets with chamber pressure 100 MPa, and nozzle diameter 1 mm. We found the impinging pressure quickly converges to an almost constant value for stand-off distances 3 mm and 6 mm, this agrees with the conclusion in Section 2. But for stand-off distance 10 mm, the flow is unstable near the impinging zone and the impinging pressure keeps fluctuating as vortices near the impinging area affect the velocity field. This suggests we may need to ensure the nozzle tracks close to the rock surface after the groove is cut. To investigate the effect of stand-off distance further, we need to run more tests for the stand-off distance between 6 to 10 mm and different chamber pressures. So far, all tests are considering flat pristine impinging plates. Of importance will be the effect of the trailing indent of the already groove-cut geometry on the impinging flow field as the jet traverse advances to extend and deepen the groove. This will be studied in the context of the rotating nozzle and geometry in simulations with Domain (B).

Fifth, also addressing objective (iv), we carried out three numerical tests for three nozzle orifice diameter 1 mm, 0.8 mm, 0.5 mm, to investigate the effect of the nozzle orifice diameter. These tests were for two cases. First, we analyse a constant chamber pressure of 100 MPa and a stand-off distance of 3 mm for all three diameters. We observed almost the same maximum impinging pressures for three nozzle orifice diameters. However, after applying 95% of the original chamber pressure (95 MPa) as a threshold to draw the impinging pressure contour, we found that the width of the pressure core decreases from 0.3 mm to 0.1 mm when the diameter decreases from 1 mm to 0.5 mm. Since the grain size of coarsest granite sample, the Sidobre granite, is in the range 2-10 mm, we must consider the effect of the microstructure at microscale. For the second case we examined the effect of decreasing the nozzle diameter when the same pump power is discharged from the nozzle, which requires different chamber pressures (and velocities) for each diameter. We discussed the potential for much higher pressures to be achieved for smaller orifice diameters when the power available is the same.

Sixth, partner Sintef measured the viscosity for base fluids of water and a bentonite/xanthan gum drilling fluid with different additive concentration (0%, 0.1%, 0.35% and 1%) over a range of shear rates. We selected five fluid rheology models to explore the possible extreme effects of different fluids, i.e., drilling fluids at 50ºC, with 0%, 0.1%, 0.35% and 1% additives, and pure water at 20 ºC. The numerical results show that impinging pressure is not sensitive to the viscosity changes (objective (iv)).

8 References

Agwu, O.E., Akpabio, J.U., Ekpenyong, M.E., Inyang, U.G., Asuquo, D.E., Eyoh, I.J., Adeoye, O.S., 2021. A critical review of drilling mud rheological models. Journal of Petroleum Science and Engineering 203, 108659. https://doi.org/10.1016/j.petrol.2021.108659

Bobo R. Method of drilling with high velocity jet cutter rock bit. Patent. United States, Patent Office; 1963

Caenn, R., Darley†, H.C.H., Gray†, G.R., 2017. The Rheology of Drilling Fluids, in: Composition and Properties of Drilling and Completion Fluids. Elsevier, pp. 151–244. https://doi.org/10.1016/B978-0-12-804751-4.00006-7

Dehkhoda, S., Hood, M., 2013. An experimental study of surface and sub-surface damage in pulsed water-jet breakage of rocks. International Journal of Rock Mechanics and Mining Sciences 63, 138–147. https://doi.org/10.1016/j.ijrmms.2013.08.013

Echt, T., Stoxreiter, T., Plank, J., 2020. Impact of the drilling fluid system on the effectiveness of a high pressure jetting assisted rotary drilling system. Heliyon 6, e04179. https://doi.org/10.1016/j.heliyon.2020.e04179

Fairweather, M., Hargrave, G., 2002. Experimental investigation of an axisymmetric, impinging turbulent jet. 1. Velocity field. Exp Fluids 33, 464–471. https://doi.org/10.1007/s00348-002-0479-7

Hahn, S., Wittig, V., Bracke, R., 2019a. Extended Horizontal Jet Drilling for EGS applications in Petrothermal Environments 4.

Hahn, S., Volker Wittig, Sarah Jasper, Dennis Schwarz, Dhafir Albadroui, Koos Hoogland, Richard R. Bakker. 2019b. Deliverable 5.2: Report on Jet drilling at simulated reservoir conditions, 2019, Potsdam: GFZ German Research Centre for Geosciences, DOI: https://doi.org/10.2312/gfz.4.8.2019.002

Hughes, T.J.R. Mallet, M. A new finite element formulation for computational fluid dynamics: IV. a discontinuity-capturing operator for multidimensional advective-diffusive systems, Comput Methods Appl Mech Eng, 58 (3) (1986), pp. 329-336, 10.1016/0045-7825(86)90153-2

Hussein, H.J., Capp, S.P., George, W.K., 1994. Velocity measurements in a high-Reynolds-number, momentum-conserving, axisymmetric, turbulent jet. J. Fluid Mech. 258, 31–75. https://doi.org/10.1017/S002211209400323X

Jasper, S., Hussong, J., Lindken, R., 2021. PIV investigation of high Reynolds number submerged water jets at high-pressure ambient conditions. Exp Fluids 62, 97. https://doi.org/10.1007/s00348-021-03167-x

Jegaraj, J.J.R., Babu, N.R., 2016. Condition Monitoring of Orifice in Abrasive Waterjet Cutting System Using High Pressure Sensor. Procedia Manufacturing 5, 578–593. https://doi.org/10.1016/j.promfg.2016.08.048

Kolle JJ. Jet kerfing parameters for confined rock. In: Proceedings of the fourth U.S. Water Jet Conference. Berkeley. 26-28 August 1987: 134–144.

Kristiawan, B., Kamal, S., Suhanan, ., Yanuar, ., 2015. A Modified Power Law Approach for Rheological Titania Nanofluids Flow Behavior in a Circular Conduit. j nanofluids 4, 187–195. https://doi.org/10.1166/jon.2015.1139

Liao, H., Guan, Z., Shi, Y., Liu, Y., 2015. Field tests and applicability of downhole pressurized jet assisted drilling techniques. International Journal of Rock Mechanics and Mining Sciences 75, 140–146. https://doi.org/10.1016/j.ijrmms.2015.01.014

Liu, S., Li, H., Chang, H., 2017. Drilling Performance of Rock Drill by High-Pressure Water Jet under Different Configuration Modes. Shock and Vibration 2017, 1–14. https://doi.org/10.1155/2017/5413823

Liu, X., Liang, Z., Wen, G., Yuan, X., 2019. Waterjet machining and research developments: a review. Int J Adv Manuf Technol 102, 1257–1335. https://doi.org/10.1007/s00170-018-3094-3

Maniadaki, K., Kestis, T., Bilalis, N., Antoniadis, A., 2007. A finite element-based model for pure waterjet process simulation. Int J Adv Manuf Technol 31, 933–940. https://doi.org/10.1007/s00170-005-0274-8

Pain, C., Umpleby, A., De Oliveira, C., Goddard, A., 2001. Tetrahedral mesh optimisation and adaptivity for steady-state and transient finite element calculations. Computer Methods in Applied Mechanics and Engineering 190, 3771–3796.

Pain, C. C., Piggott, M. D., Goddard, A. J. H., Fang, F., Gorman, G. J., Marshall, D. P., Eaton, M. D., Power, P. W., & de Oliveira, C. R. E. 2005. Three-dimensional unstructured mesh ocean modelling. Ocean Modelling, 10(1), 5-33. https://doi.org/10.1016/j.ocemod.2004.07.005

Pain, C.C. de Oliveira, C.R.E. Goddard, A.J.H. Umpleby A.P. Criticality behavior of dilute plutonium solutions, Nucl Technol, 135 (3) (2001), pp. 194-215, 10.13182/NT01-A3216

Poláček, J., Janurová, E., 2017. Impact of pressure of surrounding medium on plain water jet cutting of rocks. *Int J Adv Manuf Technol* **90,** 2185–2191 https://doi.org/10.1007/s00170-016-9554-8

Pope, S. B. 2000. Turbulent Flows. Cambridge University Press.

Schlichting H, Gersten K. Grenzschicht-Theorie. 9th ed. Berlin Heidelberg: Springer; 1997.

Sittiwong, W., Seehanam, W., Pianthong, K., Matthujak, A., Wahid, M.A., Samion, S., Sidik, N.A.C., Sheriff, J.M., 2010. Effect of Stand-Off Distance on Impact Pressure of High Speed Water Jets. Presented at the THE 10TH ASIAN INTERNATIONAL CONFERENCE ON FLUID MACHINERY, Kuala Lumpur (Malaysia), pp. 864–873. https://doi.org/10.1063/1.3464938

Smagorinsky, J. General circulation experiments with the primitive equations: I. the basic experiment, Mon Weather Rev (1963), 10.1126/science.27.693.594

Sodjavi, K., Montagné, B., Bragança, P., Meslem, A., Bode, F., Kristiawan, M., 2015. Impinging cross-shaped submerged jet on a flat plate: a comparison of plane and hemispherical orifice nozzles. Meccanica 50, 2927–2947. https://doi.org/10.1007/s11012-015-0181-5

Stoxreiter, T., Martin, A., Teza, D., Galler, R., 2018. Hard rock cutting with high pressure jets in various ambient pressure regimes. International Journal of Rock Mechanics and Mining Sciences 108, 179–188. https://doi.org/10.1016/j.ijrmms.2018.06.007

Stoxreiter, T., Portwood, G., Gerbaud, L., Seibel, O., Essl, S., Plank, J., Hofstätter, H., 2019a. Full-scale experimental investigation of the performance of a jet-assisted rotary drilling system in crystalline rock. International Journal of Rock Mechanics and Mining Sciences 115, 87–98. https://doi.org/10.1016/j.ijrmms.2019.01.011

Stoxreiter, T., Wenighofer, R., Portwood, G., Pallesi, S., Bertini, A., Galler, R., Grafinger, S., 2019b. Rock fracture initiation and propagation by mechanical and hydraulic impact. Open Geosciences 11, 783–803. https://doi.org/10.1515/geo-2019-0061

Tezduyar, T.E. Stabilized finite element formulations for incompressible flow computations, Advances in Applied Mechanics, 28, Elsevier (1991), pp. 1-44, 10.1016/S0065-2156(08)70153-4

Wang, H., Qian, Z., Zhang, D., Wang, T., Wang, C., 2020. Numerical Study of the Normal Impinging Water Jet at Different Impinging Height, Based on Wray–Agarwal Turbulence Model. Energies 13, 1744. https://doi.org/10.3390/en13071744

Xiang, J., Latham, J.-P., & Pain, C. (2019, August 28). Numerical Simulation of Rock Erosion Performance of a High-Speed Water Jet Using an Immersed Body Method. American Rock Mechanics Association. In *53rd US Rock Mechanics/Geomechanics Symposium*. Brooklyn, New York. ARMA-2019-1947. Xiang et al ARMA-2019-1947

Xiang, J., Chen, B., Latham, J.-P., & Pain, C. 2021 Numerical Simulation of Rock Erosion Performance of a High-Speed Water Jet Using an Immersed Body Method. Computers and Geotechnics (Under review).

Xiao, S., Ge, Z., Ren, Q., Liu, J., Wang, H., 2020a. Numerical analysis on the flow field structure and deflection characteristics of water jets under nozzle moving conditions. Engineering Applications of Computational Fluid Mechanics 14, 1279–1301. https://doi.org/10.1080/19942060.2020.1822210

Xiao, S., Ren, Q., Ge, Z., Chen, B., Wang, F., 2020b. Study of the rock-breaking and drilling performance of a self-rotatory water-jet bit in water-jet drilling and its influential factors. Energy Sources, Part A: Recovery, Utilization, and Environmental Effects 1–17. https://doi.org/10.1080/15567036.2020.1767732

Zhang, J., Li, Y., Zhang, Y., Yang, F., Liang, C., Tan, S., 2020. Using a high-pressure water jet-assisted tunnel boring machine to break rock. Advances in Mechanical Engineering 12, 168781402096229. https://doi.org/10.1177/1687814020962290

Zhang, Y., Zhao, Z., Huang, J., Gong, Z., Wu, W., 2011. Experimental Study of Submerged Water Jet Flow with PIV, in: 2011 Asia-Pacific Power and Energy Engineering Conference. Presented at the 2011 Asia-Pacific Power and Energy Engineering Conference (APPEEC), IEEE, Wuhan, China, pp. 1–4. https://doi.org/10.1109/APPEEC.2011.5749154

Appendix A

Python script for calculating orifice exiting velocity distribution along rotational circle

1. Fluid velocity in x direction

```
def val(X,t):
     from math import sqrt, exp, sin, cos
    val=0.0
    t1=8e-5
    length=0.0125
    a_vel=4.0*3.1415926*10.0
    xc=cos(a_vel*t)*length
    yc=sin(a_vel*t)*length
    dis=sqrt((X[0]-xc)*(X[0]-xc)+(X[2]-yc)*(X[2]-yc))
    length1=sqrt(X[0]*X[0]+X[2]*X[2])
    vel1=a_vel*length1
    if (t&lt;t1):
      val=-t/t1*(vel1*X[2]/length1)
    else:
      val=-vel1*X[2]/length1
    if (dis&gt;0.0004):
      val=0.0
    return val
```

2. Fluid velocity in z direction

```
def val(X,t):
 val=0.0
    t1=8e-5
    length=0.0125
    a_vel=4.0*3.1415926*10.0
    xc=cos(a_vel*t)*length
    yc=sin(a_vel*t)*length
    dis=sqrt((X[0]-xc)*(X[0]-xc)+(X[2]-yc)*(X[2]-yc))
    length1=sqrt(X[0]*X[0]+X[2]*X[2])
    vel1=a_vel*length1
    if (t&lt;t1):
      val=t/t1*(vel1*X[0]/length1)
    else:
      val=vel1*X[0]/length1
    if (dis&gt;0.0004):
      val=0.0
   return val
```

3. Fluid velocity in y direction

```
def val(X,t):
    from math import sqrt, exp, sin, cos
    val=0.0
    t1=8e-5
    length=0.0125
    a_vel=4.0*3.1415926*10.0
    xc=cos(a_vel*t)*length
    yc=sin(a_vel*t)*length
    y1=sqrt((X[0]-xc)*(X[0]-xc)+(X[2]-yc)*(X[2]-yc))/0.0004
    vel1=320.0
    if (t&lt;t1):
      val=-t/t1*(vel1*exp(-y1*y1/0.325))
    else:
      val=-vel1*exp(-y1*y1/0.325)
    return val
```